HHS Public Access

Author manuscript

Cell. Author manuscript; available in PMC 2024 August 17.

Published in final edited form as:

Cell. 2023 August 17; 186(17): 3686–3705.e32. doi:10.1016/j.cell.2023.07.026.

Tumor-Associated Macrophages Trigger MAIT Cell Dysfunction at the HCC Invasive Margin

Benjamin Ruf[1], **Matthias Bruhns**[2,3,4,*], **Sepideh Babaei**[2,4,*], **Noemi Kedei**[5], **Lichun Ma**[6], **Mahler Revsine**[6], **Mohamed-Reda Benmebarek**[1], **Chi Ma**[1], **Bernd Heinrich**[1], **Varun Subramanyam**[1], **Jonathan Qi**[1], **Simon Wabitsch**[1,7], **Benjamin L. Green**[1], **Kylynda C. Bauer**[1], **Yuta Myojin**[1], **Layla T. Greten**[1], **Justin D. McCallen**[1], **Patrick Huang**[1], **Rajiv Trehan**[1], **Xin Wang**[1], **Amran Nur**[1], **Dana Qiang Murphy Soika**[1], **Marie Pouzolles**[8], **Christine N. Evans**[9], **Raj Chari**[9], **David E. Kleiner**[10], **William Telford**[11], **Kimia Dadkhah**[12], **Allison Ruchinskas**[12], **Merrill K. Stovroff**[13], **Jiman Kang**[13], **Kesha Oza**[13], **Mathuros Ruchirawat**[14,15], **Alexander Kroemer**[13], **Xin Wei Wang**[6,16], **Manfred Claassen**[2,3,4,#], **Firouzeh Korangy**[1,#], **Tim F. Greten**[1,16,#,¥]

[1]Gastrointestinal Malignancy Section, Thoracic and Gastrointestinal Malignancies Branch, Center for Cancer Research, National Cancer Institute, National Institutes of Health, Bethesda, Maryland, USA.

[2]Department of Internal Medicine I (Gastroenterology, Gastrointestinal Oncology, Hepatology, Infectious Diseases and Geriatrics), University Hospital Tübingen, Tübingen, Germany

[3]Department of Computer Science, University of Tübingen, Tübingen, Germany

[4]University of Tübingen, Interfaculty Institute for Biomedical Informatics (IBMI), Tübingen, Germany

[5]Collaborative Protein Technology Resource, OSTR, Office of the Director, Center for Cancer Research, National Cancer Institute, National Institutes of Health, Bethesda, Maryland, USA.

[6]Laboratory of Human Carcinogenesis, Center for Cancer Research, National Institutes of Health, National Cancer Institute, Bethesda, Maryland, USA.

[7]Department of Surgery, Medical University of Vienna, Vienna, Austria

[¥]Lead contact: Tim F. Greten, GI Malignancy Section, Thoracic and GI Malignancies Branch, NIH/NCI/CCR Building 10, Rm 2B38B, 9000 Rockville Pike, Bethesda, MD 20892, U.S.A., Phone: +1 (240) 760 6114, tim.greten@nih.gov.

[*]These authors contributed equally

[#]Senior author

AUTHOR CONTRIBUTIONS

Conceptualization, B.R., A.K., M.C., F.K., T.F.G.; Methodology, B.R., M.B., S.B., N.K., A.K., M.C., F.K., T.F.G.; Software: M.B., S.B., M.C.; Validation, L.M., M.R., X.W.W.; Investigation: B.R., M.B., S.B., N.K., C.M., B.H., V.S., J.Q., S.W., B.L.G., K.C.B., Y.M., M.R.B., L.T.G., J.D.M., P.H., R.T., X.W., A.N., D.Q.M.S., M.P., C.E., R.C., D.K., W.T., K.D., A.R., M.K.S., J.K., K.O.; Formal Analysis: B.R., M.B., S.B., M.C., N.K., L.M., M.R., C.M., M.C., F.K., T.F.G.; Writing – Original Draft: B.R., F.K., T.F.G.; Writing – Review & Editing: all authors, Visualization: B.R., M.B., S.B., N.K.; Funding Acquisition: A.K., X.W.W., M.C., T.F.G; Resources: M.R.; Supervision: M.C., F.K., T.F.G.

DECLARATION OF INTEREST

The authors declare no competing interests.

[8]Pediatric Oncology Branch, Center for Cancer Research, National Cancer Institute, National Institutes of Health, Bethesda, Maryland, USA.

[9]Genome Modification Core, Frederick National Lab for Cancer Research, Frederick, Maryland, USA.

[10]Laboratory of Pathology, Center for Cancer Research, National Cancer Institute, National Institutes of Health, Bethesda, Maryland, USA.

[11]Experimental Transplantation and Immunotherapy Branch, Center for Cancer Research, National Cancer Institute, National Institutes of Health, Bethesda, Maryland, USA.

[12]Single Cell Analysis Facility, Cancer Research Technology Program, Frederick National Laboratory, Bethesda, MD, USA.

[13]MedStar Georgetown Transplant Institute, MedStar Georgetown University Hospital and the Center for Translational Transplant Medicine, Georgetown University Medical Center, Washington, DC, USA.

[14]Laboratory of Chemical Carcinogenesis, Chulabhorn Research Institute, Bangkok, Thailand.

[15]Center of Excellence on Environmental Health and Toxicology, Office of the Higher Education Commission, Ministry of Education, Bangkok, Thailand.

[16]NCI CCR Liver Cancer Program, National Institutes of Health, Bethesda, Maryland, USA.

SUMMARY

Mucosal-associated invariant T (MAIT) cells represent an abundant innate-like T cell subtype in the human liver. MAITs are assigned crucial roles in regulating immunity and inflammation, yet their role in liver cancer remains elusive. Here, we present a MAIT-centered profiling of hepatocellular carcinoma (HCC) using scRNA-seq, flow cytometry, and co-detection by indexing (CODEX) imaging of paired patient samples. These analyses highlight the heterogeneity and dysfunctionality of MAITs in HCC and their defective capacity to infiltrate liver tumors. Machine learning tools were used to dissect the spatial cellular interaction network within the MAIT neighborhood. Co-localization in the adjacent liver and interaction between niche-occupying $CSF1R^{+}PD\text{-}L1^{+}$ tumor-associated macrophages (TAMs) and MAITs was identified as key regulatory element of MAIT dysfunction. Perturbation of this cell-cell interaction in *ex vivo* co-culture studies using patient samples and murine models reinvigorated MAIT cell cytotoxicity. These studies suggest that aPD-1/aPD-L1 therapies target MAITs in HCC patients.

Graphical Abstract:

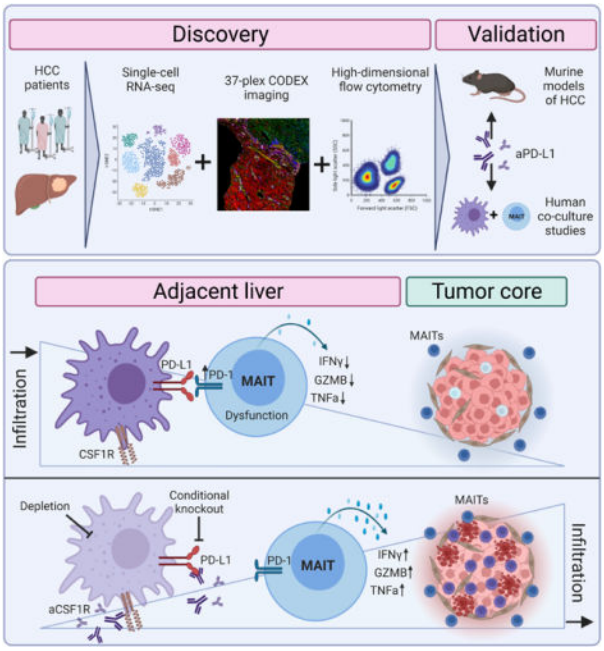

IN BRIEF

Insights into the functions of an underappreciated type of immune cell, the mucosal-associated invariant T cell (MAIT), and how the immunosuppressive tumor microenvironment restrains these cells, with potential implications for treating hepatocellular carcinoma with cancer immunotherapy.

Keywords

Mucosal-associated invariant T cells (or MAITs); tumor-associated macrophages; HCC; CODEX; S^3-CIMA; aPD-1/aPD-L1

INTRODUCTION

Hepatocellular Carcinoma (HCC) is an inflammation-derived cancer typically caused by chronic liver injury[1]. The cellular composition of the HCC tumor immune microenvironment (TiME) influences tumor initiation, progress, and response to therapy[2]. Immune checkpoint blockade (ICB) therapies exist for treating advanced HCC[3]. Nevertheless, only a limited number of patients shows substantially improved clinical outcome, partly due to a hostile TiME dampening conventional T cell responses[4].

MAIT cells are MR1-restricted innate-like T cells that recognize non-peptide antigens, including derivatives of microbiota-derived vitamin B2 (riboflavin) precursors[5]. While MAITs represent an overabundant T cell subtype in the healthy human liver and can comprise up to 45% of intrahepatic T cells[6], their frequency is ~100-fold lower in laboratory mice[7].

Whether MAIT cells promote cancer or contribute to anticancer immunity remains unstudied. Increased MAIT cell numbers in HCC tumors and altered MAIT cell function have been correlated with poor clinical outcome[8]. In contrast, higher MAIT cell infiltration correlated with a favorable prognosis within a cohort of cholangiocarcinoma patients[9].

Functional studies in murine cancer models have recently corroborated the role of MAITs in the TiME as a double-edged sword: MAITs appear pathogenic as MAIT deficient *Mr1*$^{-/-}$ mice had favorable outcomes in models of lung metastasis and subcutaneous tumors[10]. However, we and others have demonstrated that MAIT cells also elicit protective roles and contribute to anti-tumor activity in mice when activated with a MAIT-TCR ligand, 5-OP-RU (5-(2-oxopropylideneamino)-6-D-ribitylaminouracil)[11,12]. Polarized MAIT cells produce more T_H1-cytokines (including IFNγ) and express more cytolytic effector molecules, making them potentially useful in anti-tumor immunity[11,12].

The factors that determine MAIT cell fate in hepatocarcinogenesis remain largely unknown, although, context-dependent effector functions of MAITs may explain their dichotomous properties. Furthermore, little is known about the MAIT cell interaction network within the TiME contributing to their dysfunction or anti-tumor activity.

In this study, we profiled human and murine MAIT cells in liver cancer using co-detection by indexing (CODEX) immunofluorescence imaging, high-dimensional flow cytometry and single-cell RNA sequencing. MAITs in liver cancer were generally characterized by an impaired infiltration into tumors as well as increasing dysfunction/loss-of-cytotoxicity within the HCC TiME. We applied S^3-CIMA, a recently described representation learning method, to analyze the spatially resolved, CODEX-derived immune cell atlas of human liver cancer and identified PD-L1$^+$ TAMs as key interacting players in the MAIT cell neighborhood in the adjacent liver. Perturbation of this TAM-MAIT interaction in various murine models of liver cancer and *ex vivo* co-culture studies using patient samples reinvigorated the anti-tumor MAIT cell phenotype. The translational aspect of these findings is further demonstrated as aPD-1/aPD-L1 ICB reversed the MAIT cell dysfunctionality in co-culture studies and murine models of HCC.

The present work unravels the spatio-temporal factors contributing to MAIT cell heterogeneity and increasing dysfunction in HCC suggesting them as potential effector cells of PD-L1/PD-1-directed ICB in HCC.

RESULTS

scRNA-seq profiling of the tumor immune landscape in HCC

To characterize MAIT cells within the overall immune landscape in our HCC cohort (Study design, see STAR METHODS, Fig. S1 and Table S1), we applied scRNA-sequencing to sorted CD45$^+$ mononuclear cells (MNCs) isolated from matched tumors and adjacent liver tissue from 8 patients with histologically confirmed HCC undergoing surgical resection (See sorting strategy Fig.S2A).

Consistent with published scRNA-seq data on HCC[13,14], differentially expressed gene (DEG) analysis (Table S1) identified major immune cell clusters of myeloid cells including macrophages and dendritic cells (c8 & c11; characterized e.g. by *LYZ, and CD68 or CD1C* expression), pDC (c18), DC1 (c16; *CLEC9A*), T cells (c1, c4, c5, c6, c7, c10, c12, c14) expressing *TRAV* or *TRBV* or *CD3E/CD3D/CD3G*), B cells (c13; *CD79A, MS4A1*), and natural killer (NK) cells (c2, c3, *GNLY, KLRB1* or *FCGR3A*) and an ILC cluster (c17, *IL7R, GATA3, KIT, KLRB1*) (Figs.1A-D and Fig.S2B). One cluster consisted of cycling immune cells (c15; *MKI67 & PCNA*).

Within the T cell compartment, several clusters of $CD4^+$ helper and $CD8^+$ cytotoxic T cells, one cluster of regulatory T cells (c12; *FOXP3, CTLA4*as well as one distinct MAIT cell cluster (c9), were identified. In line with known MAIT cell genes[15,16], this MAIT cell cluster had high expression of MAIT cell-defining TCR alpha and beta chain transcripts *TRAV1–2, TRBV20–1, TRBV6–4, TRBV6–1 as well as SLC4A10, RORC, CCL20, IL7R, CCR6 and KLRB1* expression (Fig.1D, Table S1). The major MAIT cell cluster c9_MAIT was represented at significantly higher frequency in the adjacent liver tissue as compared to the tumor-infiltrating T cells (p= 0.0078, Fig.1E).

All major immune cell types were shared among patients (Fig.1B). Significant differences were observed between the adjacent liver tissue and tumor core (Fig.1C), albeit at varying proportions (Fig.S2C&D). c4_CD8_GZMK cytotoxic T cells, c3_NK_CD56 and c9_MAIT cell cluster were significantly reduced in the tumor-derived samples. On the other hand, T_{regs} (c12_Tregs) and cycling cells (c15_cycling) were more abundant in the tumor core. Frequencies of immune cell clusters varied among patients, revealing a substantial heterogeneity in the immune cell composition of HCC (Fig.S2C).

MAIT cell gene signature is associated with better survival in HCC patients

We sought out to determine a correlation between MAIT cell infiltration and patient survival in HCC patients by applying the scRNA-seq derived MAIT-cell gene signature to previously published bulk sequencing datasets for HCC patients. Yao et al recently demonstrated the robustness of a MAIT cell gene signature to correlate with MAIT cell infiltration[15]. This signature had 11/11 genes overlap with the main MAIT cell cluster c9_MAIT (Fig.1A, Table S1) and we used both signatures to assess overall survival in a large independent HCC cohort (TCGA). Prolonged overall survival was found in patients stratified by high expression of both transcriptomic MAIT cell signatures in tumor samples in the TCGA cohort. (Fig.1F&G).

Single-cell RNA sequencing reveals MAIT cell heterogeneity within the HCC bearing liver

To study MAIT cells in greater depth, we selected MAIT cells from $CD45^+$ sorted cells based on the expression of the semi-invariant TCRα-chain (TRAV1-2-TRAJ33/12/20)[15].

Since MAIT cells were scarce in HCC tumors (Fig.1E) further enrichment was necessary to investigate MAIT cell heterogeneity at greater resolution. We FACS sorted additional MAIT cells (see sorting strategy in Fig.S2A) from 6 patient samples. Unsupervised clustering revealed the heterogeneity within the MAIT cell population. MAIT cells clustered into six distinct (sub-) clusters (Fig.1H, TableS1) shared amongst patients with varying degrees of

location preference (Fig.S3A&B). The MAIT cell subclusters had varying levels of NK cell related genes, pro-inflammatory cytokines (*IFNG*) and cytotoxic effector molecules mainly expressed in clusters m1–4. MAIT subcluster m5 showed upregulation of genes indicative of dysfunction or exhaustion (Fig.1I, Fig.S3C). This dysfunctional MAIT subcluster, m5, also expressed higher levels of FOXP3, CXCR3 and CD4, resembling transcripts from regulatory T cells, in line with a recent study of anergic MAIT cells in colorectal cancer[17]. One small subset of MAITs (cluster m6) were proliferating as indicated by high expression of *MKI67*. We next investigated an independent scRNA-seq of sorted T cells from HCC patients[16]. Subclustering of the main MAIT cell cluster, C3__(CD8-SLC4A10) idenfied a subset of MAITs (z4) with upregulation of genes associated with T cell dysfunctionality in cancer (e.g. *CTLA4, ICOS* and *PDCD1,* Fig.S3D) and lower expression of genes associated with NK cells or cytotoxicity (*NCR3, NKG7*, *GNLY, PRF1, GZMB, GZMH, GZMK,* Fig.S3E). The differentially expressed genes from the z4 dysfunctional MAIT cell cluster[16] had high correlation with the dysfunctional MAIT cell cluster m5 from our HCC patient cohort (Fig.S3F).

Human MAIT cells are aberrantly activated and show an increasingly dysregulated phenotype within the HCC TiME

To confirm the above findings, we assessed MNCs derived from matched tumors and adjacent non-tumor tissues from n=37 patients by flow cytometry (Fig.2A&B, **gating strategy** Fig.S4A). Similar to the scRNA-seq dataset and recent reports[8], MAIT cell infiltration into HCC lesions was significantly impaired relative to matched non-tumor adjacent liver (Fig.2C). While the majority of hepatic MAIT cells in our patient cohort were predominantly $CD8^+$ or double negative (DN), an increasing proportion of tumor-infiltrating MAIT cells were $CD4^+$ (Fig.S4B). Additionally, human MAITs in HCC lesions showed signs of activation/dysfunction as measured by increased expression of PD-1, CD25 & HLA-DR (Fig.2D & Fig.S3C) and down regulation of NK cell marker CD56 (Fig.2D). While CD38 (Fig.S4C) expression was unaffected, CD69 was expressed on the vast majority of MAIT cells in both tumor and adjacent liver considered a marker of tissue residency rather than activation[18].

We assessed the MAIT phenotype from an additional set of (n=23) samples from patients with chronic liver disease but without malignancy to determine if changes in MAITs were induced by underlying liver disease or presence of the tumor. Similar to previous studies[19], hepatic MAIT cells from patients with chronic liver disease had significantly lower levels of PD-1 expression and higher levels of CD56, of MAIT cells in the absence of HCC (Fig.S4D).

Loss of cytotoxicity in murine MAIT cells in response to liver tumor growth

Human and murine MAIT cells differ in terms of abundance, phenotype, and transcription factors[20], e.g. their frequency in hepatic T cells at homeostasis is up to 100 fold lower in mice compared to human (Fig.S4E).

We studied the changes in MAIT cell phenotype in response to tumor growth using several syngeneic models of murine orthotopic liver cancer. Murine tumor cell lines RIL-175,

Hep55.1c, MC38 and B16-F10[12] were surgically implanted into mouse livers, followed by analysis of hepatic and tumor infiltrating leukocytes (Fig.2E). Mimicking findings in human, murine MAIT cell infiltration (gating strategy see Fig.S4E) into liver tumors was significantly impaired across all tumor cell lines tested (Fig.2F). In addition, MAIT cells in the HCC-bearing livers also acquired a late dysfunctional phenotype[21] characterized by high expression of PD-1 and TIM-3 (Fig.2G for RIL-175 and Fig.S4F for Hep55.1c) mirroring the findings as observed in human HCC samples. CD69 expression on murine MAITs remained unchanged. These dysfunctional MAIT cells also had altered transcription factor profiles: While hepatic MAIT cells at homeostasis were predominantly T-bet^{+}RORγt^{-}, HCC presence in murine livers induced a phenotypic switch from T_H1-like to a T_H17-like phenotype in MAIT cells with increased expression of RORγt and significant reduction in T-bet expression (Fig.2H). Enhanced levels of proliferation marker Ki-67 (Fig.S4G) and reduced frequency of apoptotic MAITs (Fig.S4H) indicated that impairment of MAIT cell infiltration into liver tumors was not due to a lack of proliferation or enhanced rate of cell death. Finally, intrahepatic tumor growth resulted in MAIT cells that lack pro-inflammatory cytokines IFNγ and TNFα, with reduced frequency of granzyme B^{+} (Fig.2I).

We next studied the phenotypic changes in hepatic immune cell populations in mice without an underlying liver condition, allowing us to specifically attribute alterations in MAIT cell function to HCC. Progressive HCC outgrowth in this model was induced by overexpression of *Myc* and deletion of *p53*[22] (Fig.S4I-J). We observed increasing MAIT cell dysfunction over time (2 vs. 4 weeks) as measured by pronounced PD-1 expression and loss of pro-inflammatory IFNγ production (Fig.S4J vs. K).

In summary, MAITs in human and murine HCC were characterized by impaired infiltration into liver tumors, a gradual dysfunction, and a marked heterogeneity within the HCC TiME.

Tumor-induced dysfunction of murine hepatic MAIT is independent of tumor MR1 expression

A recent study attributed tumor-promoting function of murine pulmonary MAIT cells to the direct interaction between MAIT-TCR and MR1 on tumor cells[10]. We tested MR1 surface expression at baseline as well as after incubation with MR1-ligand, 5-OP-RU, on the tumor cells. B16-F10 was the only tumor cell line that showed detectable MR1 surface expression upon stimulation (Fig.S4L) as shown previously[10]. To test whether the dysfunctional phenotype of intrahepatic tumor MAIT cells was through tumor-MR1 engagement with the MAITs, we used an *Mr1*-deficient murine B16-F10 cell line[12]. Intrahepatic B16-*Mr1*$^{-/-}$ tumor growth also led to comparable MAIT cell phenotypic changes as measured by expression of surface markers PD-1, TIM-3 and CD69 (Fig.S4M) as well as changes in RoRγt (upregulation) and T-bet (downregulation, Fig.S4N).

These findings suggest that the acquired MAIT cell dysfunction in liver cancer is independent of MR1 expression on tumor cells and likely mediated by interacting cell partners within the immunosuppressive TiME of HCC.

MAIT-deficient Mr1$^{-/-}$ mice have reduced intrahepatic tumor burden compared to WT mice

Next, we implanted two different syngeneic murine tumor cell lines (Hep55.1c and MC38) into the livers of wildtype or MAIT-deficient *Mr1*$^{-/-}$ knockout mice (Fig.2J; Fig.S4E) to see whether hepatic MAITs can contribute to the control of intrahepatic tumors. *Mr1*$^{-/-}$ mice showed larger intrahepatic tumors (Fig.2K–M), indicating that hepatic MAIT cells indeed contribute to tumor immunosurveillance in murine livers.

Generation of a spatially resolved immune cell atlas of human liver cancer by CODEX technology

To characterize the composition of the MAIT cell niche in human liver cancer and identify potential interacting partners, we generated a spatially resolved immune cell atlas of human liver cancer using CODEX[23] technology (Fig.3A). A multiplexed imaging dataset on n=15 sections from human HCC specimen (including eight matched samples from the scRNA-seq dataset, TableS1) was generated using a specifically developed and validated panel of 37 oligonucleotide-barcoded antibodies (Fig.3A, TableS1, and Fig.S5).

We imaged the entire tissue section for each sample in whole slide scanning technique, encompassing the full range of the tumor-to-liver interface and the differential analysis between adjacent (non-tumor) liver tissue, HCC invasive margin (rim) and tumor core within the same tissue section (Fig.3B). Surgical resection specimens contain a broad range of histopathologically distinct areas (Fig.3C) ranging from seemingly unaffected liver parenchyma with liver sinusoids covering lines of hepatocytes (Fig.3C, ①), portal triads (Fig.3C, ②), lymphocyte aggregates consistent with tertiary lymphoid structures (TLSs, Fig.3C, ③), as well as proliferating tumor cells within areas of neovascularization (Fig.3C, ④). This approach allowed us to determine the composition of the MAIT cell niche across different hepatic compartments and to infer interactions between cell types.

Single-cell segmentation and cell annotation

Highly multiplexed CODEX imaging represents a powerful tool for spatially resolved single-cell analysis[24]. We developed an image analysis pipeline that is displayed in Fig.3B, Fig.S6A–D (see STAR Methods). A total of 4,567,421 cells were identified and annotated.

The numerical data generated based on cell segmentation provided in the form of spatial feature tables was used for intensity-based unsupervised clustering. To construct a global HCC TiME atlas, we performed cell identification based on all 38 available markers to annotate cell types with low granularity (Fig.S7A–D). Annotation of clusters was guided by the expression levels of canonical protein markers and visual inspection of the raw images (heatmap in Fig.S7E). Notably, tumor cells from individual patients clustered often in a patient-specific manner (Fig.S7A–C) while common parenchymal and immune cell types were derived from all patients. The unsupervised clustering also revealed rare cell types, e.g. a small cluster of NCAM^{+} (Neural cell adhesion molecule or CD56) cells was identified (Fig.S7F). Backtracking these cells in the raw image revealed that they were mainly located within in the walls of large vessels in the adjacent liver, indicating that they belong to neurons innervating the smooth muscle layer of hepatic arteries (Fig.S7F). Quantification of the different (gross) cell types across different tissue regions is displayed in Fig.S7G.

For immune cell clustering, 1,558,175 $CD45^+$ leukocytes were selected and re-clustered resulting in a total of 20 distinct immune cell clusters and one cluster with mixed immune cells (Fig.4A, STAR Methods). Adjacent liver, rim and tumor core shared the major immune cell subtypes and little patient-specific clustering could be observed (Fig.4B&C). Key immune cell markers projected onto distinct regions of the UMAP space (Fig.4D).

The heatmap in Fig.4E shows characteristic CODEX protein expression of the different leukocyte clusters. Within the myeloid-cell fraction, two clusters of granulocytes were identified that were distinguished by the expression of CD38. Macrophages were identified by expression of CD68 with Kupffer cells being $CD163^-CD39^-$ and two clusters of TAMs ($CD163^+CD39^+$) could be separated by PD-L1 expression levels. A cluster of HLA-DR^+ antigen-presenting cells (APCs) likely comprised dendritic cells as well as macrophages. In line with the scRNA-seq dataset, two natural killer (NK) cell clusters likely correspond to circulating ($CD16^{high}$) and tissue resident NK cells ($CD56^{high}$) were seen[25]. A total of nine T cell clusters were delineated: one MAIT cell cluster (containing 44,733 cells), one T_{reg} cluster, one CD8 T cell cluster with a late dysfunctional phenotype (PD-$1^{high}CD39^+$) and distinct from CD8 T PD-1^{low} cells. The $CD4^+$ and $CD8^+$ clusters indicated PD-L1 expression, but close inspection of the CODEX images clearly showed that the PD-L1 signal was rather derived from a neighboring cell and can thus be considered due to lower performance of the segmentation algorithm. Absence of PD-L1 expression on T cells was confirmed by flow cytometry (not shown). Naïve CD4 T cells were distinct from the remaining CD4 T cell clusters by expression of CD62L and CD45RA. $CD57^+$ T cells consisted of both CD4 and CD8 subsets. Three B cell clusters were distinguished by expression of CD38, PD-L1 and CD45RA.

These findings show that MAIT cells can be identified in intact tissue based on the expression on TCRVa7.$2^+CD161^+CD69^+$ which allowed us to perform further spatial analysis.

Leukocyte subpopulations show distinct infiltration patterns into HCC tumors

CODEX images can be analyzed using spatial X/Y-coordinates of each cell in the intact tissue context. This was used to further evaluate the leukocyte composition in distinct histopathologic regions of HCC: adjacent liver, rim and tumor core. Notably, global leukocyte density increased at the tumor interface (rim) and was significantly higher compared to the tumor core region (Fig.4F). Overall, immune cell frequencies as determined by CODEX imaging paralleled the trends seen in the flow cytometry analyses and showed significant correlation (Fig. 4G), with the strongest correlation found for MAITs. Comparison of the two phenotyping strategies (i.e. manual gating vs. unsupervised clustering) (Fig.S7H) led to comparable results as recently demonstrated[26].

Spatial mapping revealed that among leukocyte subpopulations, different overall trends in tumor infiltration patterns could be observed (Fig.4H, Sankey diagram, Fig.S8). B cell subsets, $CD56^+$ NK cells, $CD38^+$ granulocytes, $CD4^+$ and $CD8^+$ T cell subsets as well as MAITs followed overall trends of total leukocytes with a marked accumulation at the rim region and lowest densities within the tumor core (Fig.4H, Fig.S8).

Noticeable spatial dynamics in terms of relative abundance of different leukocyte subpopulations across tissue categories were noted: while CD8 T PD-1^{low} cells, TAMs expressing PD-L1, CD4 T cells and CD38^{-} granulocytes were the dominant fractions in the adjacent liver, MHCII^{+} APCs, CD4 T cells, late dysfunctional PD-1^{high} CD8^{+} T cells and regulatory T cells presented with highest frequencies in tumor core regions (Fig.4H, **pie charts**).

Collectively, spatial mapping of leukocyte subsets revealed dynamic differences in the composition and cellular functional subsets within the TiME. Mapping of MAIT cells show marked alterations in cellular density at the HCC invasive margin in the immediate vicinity of the tumor which was further investigated as a region of particular interest.

The HCC invasive margin as the localization of spatially resolved immune cell activation/ inhibition

The dynamic changes in the TiME in both frequency and cellular densities within the spatial categories of the tissue sections (i.e. within ~1cm of the invasive margin of HCC tumors) highlight the importance of histological location and tissue area in tumors[27]. We reasoned that the tumor-to-liver interface was a region where multicellularity and cellular crosstalk confer cellular immune cell function.

CODEX imaging revealed non-random heterogeneity of cell type distribution as well as functional immune cell markers within the distinct tissue regions of the tumor-to-liver interface (Fig.S9A). MAIT cells were found to accumulate at the rim region (Fig.S9B) with a low density of MAITs in HCC tumors (Fig.S9C). CD4^{+}, CD8^{+} T cells and NK cells showed similar migratory impairment at the immediate tumor border. However, Tregs showed similar densities 500 μm outside the tumor border and 500 μm inside the tumors (mean of 29.3 vs. 28.1 cells/mm^{2}).

Beyond migratory capacities, functional states of immune cells can be approximated by expression levels of key markersindicating activation, proliferation, or dysfunction (PD-1, CD25, ICOS, CD39 and Ki-67)[28] (Fig.S9D). Ki-67 levels steadily increased on MAITs, CD4^{+} T cells, CD8^{+} T cells and NK cells from adjacent liver towards the tumor core. Tumor-infiltrating MAIT cells showed a significant increase in activation markers, CD25 and ICOS and higher (by trend) levels of PD-1 and CD39, matching flow cytometry as well as scRNA-seq data (Fig.1I and Fig.2D). All lymphocyte subsets generally showed similar trends towards higher expression levels of these markers from adjacent liver towards the tumor core.

Therefore, CODEX imaging of the tumor-to-liver interface revealed dynamic changes in both cellular distribution and function of MAIT cells within the immune landscape in HCC at high spatial resolution. Our findings indicate dysfunctionality of MAIT cells and other immune effector cells that is already initiated outside of the immediate tumor region. Our findings also highlight that lymphocyte dysfunctionality is a gradually acquired process rather than a binary cell state, which is accelerated at the immediate vicinity of the tumor border.

S^3-CIMA identifies the cellular interaction network within the MAIT cell niche

So far, we characterized the MAIT cells in HCC by impaired infiltration into HCC tumors, aberrant activation/dysfunction paired with a loss of cytotoxicity. We hypothesized that MAIT cell impairment might be derived from deleterious cell-cell interactions. We spatially mapped immune cell associations and calculated cellular densities around MAITs (Fig.S10A). Calculation of average Euclidian distances between MAIT cells and other immune clusters showed that these results were heavily affected by overall densities of the interacting cells. E.g., lower $CD16^+$ NK cell (and MAIT cell) densities in the tumor resulted in larger average distances in this tissue region compared to the adjacent liver (Fig.S10B). The opposite was found for MAIT-T_{reg} distances which was affected by a significantly higher T_{reg} density in the tumor (Fig.S10B).

While abovementioned proximity analyses allowed for a simple description of the MAIT cell neighborhood in liver cancer, it did not capture preferential spatial interactions between MAIT cells and other cell types beyond random distribution. Thus, we sought out to elucidate how higher-order properties of cellular organization within the HCC tumor microenvironment shape and constrain MAIT cell function.

We recently developed S^3-CIMA[29], a supervised, spatially informed representation learning method implementing *multiple instance learning*[30] paradigms with a *convolutional neural network* (CNN) model[31] (S^3-CIMA input and architecture are displayed in Fig.5A). To identify the characteristic cell state composition of the MAIT cell niche in HCC, S^3-CIMA multi-cell inputs comprised spatial nearest neighbors of MAIT cells in different tissue categories (whole tissue, adjacent liver, rim & tumor core). Spatially enriched cell subsets indicate MAIT-specific association in the respective spatial compartment (Fig.S11A, STAR Methods). K=40 nearest neighbors was found to yield best classification accuracy and discrimination of the MAIT neighborhood signatures between the tissue compartments (Fig.5B).

The MAIT-centered S^3-CIMA analysis allows for identification and characterization of tissue-specific cell populations in the MAIT niche with respect to their differential molecular profile. We found that neighboring cells derived from adjacent liver and rim were selected at significantly higher frequencies compared to background and cells from tumor core (Fig.5B). These findings indicate that MAIT-specific cellular interactions already occur outside the tumor. Interpretation of the selected cell populations based on previously assigned cell annotations revealed the cellular interaction network of the MAIT cell niche in the HCC adjacent liver (Fig.5C & D). The total number of cells of a given annotated cell type in the MAIT neighborhood did not correlate with a higher enrichment score (Fig.5D). Instead, when computed for the adjacent liver, only few subsets showed enrichment ($ES \geq 1$) within the MAIT cell niche in the adjacent liver (Fig.5C & D). Computed over the whole tissue sections, TAMs were the only cell subset that showed MAIT niche-specific enrichment across adjacent liver, rim, and tumor core (Fig.S11B & C). Interestingly, $CD163^+$ TAMs have previously been associated with poor survival in HCC patients[32] with one mechanism of action being PD-L1-mediated suppression of $CD8^+$ T cells[33]. We reasoned that these properties of $CD163^+$ TAMs made them a putative interaction partner of MAIT cells. Findings from S^3-CIMA analysis were confirmed by visual inspection of

the image data as MAIT cell interaction with PD-L1^{+} TAMs was frequently observed within the liver sinusoids of the adjacent liver tissue (Fig.S11D). These MAIT PD-1 - TAM PD-L1 interactions were found in all patient samples (examples shown in Fig.5E). CODEX microscopy images revealed that PD-1 on MAIT cells localized preferentially towards the immune synapse. MAIT cell interaction with PD-L1^{+} cells can be approximated by measuring PD-L1 intensity on MAIT cells, even though MAITs did not express PD-L1 themselves (Fig.S11E). In line with the S^{3}-CIMA analysis, this potentially unfavorable interaction occurred in the adjacent liver and rim rather than the tumor core (Fig.S11E). Beyond the enrichment in the MAIT cell neighborhood, PD-L1^{+} TAMs were among the cells with the highest expression of PD-L1 in the adjacent liver (Fig.5F). Analysis of HCC patient samples by flow cytometry confirmed that macrophages (defined as CD45^{+}CD68^{+}) were already polarized towards an M2-phenotype (CD163^{high} and PD-L1^{high}) in the adjacent liver (Fig.5G).

In summary, CODEX imaging revealed coordinated transitions between MAIT phenotypic states initiated outside the tumor. Dynamic MAIT phenotypes could be delineated based on the co-localization and functional state (PD-L1 expression) of niche-occupying CD163^{+} TAMs.

CD163^{+}PD-L1^{+} TAMs impair human MAIT cell function ex vivo

Next, we established an *ex vivo* co-culture system using freshly isolated, hepatic CD163^{+} -sorted macrophages and sorted MAIT cells from patient samples to test whether hepatic CD163^{+} macrophages can suppress MAIT cell function (Fig.6A). This *ex vivo* assay showed that co-culture with purified CD163^{+} macrophages, but not with CD163^{-} hepatic immune cells impaired IFNγ production by hepatic MAIT cells (Fig.6B-C). Co-culture using a transwell-system showed that suppressive function of CD163^{+} macrophages was cell-contact dependent (Fig.6D). Purified CD163^{+} macrophages showed high expression of PD-L1 compared to CD163^{-} cells (Fig.6E), and *in vitro*-blockade of the MAIT-TAM interactions using aPD-L1 antibody partially restored MAIT IFNγ production (Fig.6F). These studies demonstrate that human hepatic CD163^{+} macrophages inhibit liver MAIT cell function through a cell-contact and PD-L1 dependent mechanism.

MAIT cells are a potential target of aPD-1/aPD-L1-based ICB in liver cancer patients

The *in vitro* experiments suggested that human hepatic MAIT cells could be targeted by aPD-1/aPD-L1-based ICB. Whether this also applies to liver cancer patients undergoing ICB is unknown. Thus, we compared hepatic and tumor-infiltrating MAIT cells in core-needle biopsies from 8 patients with HCC treated with ICB. We compared baseline (prior to treatment initiation) and subsequent biopsy samples (after treatment) by single-cell RNA-sequencing (Fig.S12A,[34]). MAIT cell cluster in scRNA-seq data was identified by unsupervised clustering as outlined in Fig.1. (DEG list for the MAIT cell cluster in the Ma et al. dataset shown in Table S1). MAIT cells in clinical biopsy specimens expanded upon aPD-1/aPD-L1 therapy both as a fraction of all immune cells and as a percentage of total T cells in 5/8 patients (Fig.S12B). While expansion among T cells and all immune cells did not reach statistical significance in this small cohort, MAIT cell cytotoxicity was recovered as seen by a significantly increased cytotoxicity score (Fig.S12C).

Characterization of human and murine TAMs in HCC

As described above, the potential interaction of PD-L1^{+}CD163^{+} TAMs with MAIT cells was discovered using the CODEX dataset which provides rich spatial information but is limited in the number of protein markers. As scRNA-seq and CODEX were performed on paired patient samples, we sought out to integrate both high-dimensional datasets. This approach allowed for the mapping of gross immune cell clusters from CODEX onto corresponding scRNA-seq clusters,but was found limited in terms of resolution. E.g. CODEX cluster PD-L1^{+} TAM had high correlation with both myeloid cell clusters c8_Myeloid - HLA-DRA and c11_Myeloid – FTL (Fig.S12D).

To increase the resolution of this analysis and to identify additional markers that characterize the immunosuppressive CD163^{+}PD-L1^{+} macrophage population, myeloid cell clusters derived from Fig.1A were selected and re-clustered. This defined six distinct myeloid cell subsets which corresponded to previously described myeloid subsets in HCC[13,14] (Fig.6:G&H): two dendritic cell clusters: c1-DC-CD1C in accordance with “DC-c1-CD1C”[13] and “DC2”[14] and c5-DC-CLEC9A in line with “DC-c3-CLEC9A”[13] and “DC1”[14] as well as c6-pDC (also in[14]). c4-Mono-ZFP36 had high expression of CCL5 and IL32, like previously described monocyte subsets: “Mono 2”[14]. The macrophage compartment was divided into two clusters c2-Mφ-S100A9 showing overlap with “Mφ-c6-MARCO”[13] and c3-Mφ-C1QA in line with “Mφ-c2-C1QA”[13]. Both Mφ clusters were characterized by *LYZ, CD14, ITGAM and CD68* but higher levels of *CD163* could be found in c3-Mφ-C1QA. While the transcript for *CD274* (encoding for PD-L1) was not detected in the human scRNA-seq dataset, cluster c3-Mφ-C1QA showed high expression of other genes associated with an immunosuppressive or “M2” phenotype like *MRC1* (encoding for CD206), *TREM2* and *CSF1R* (Fig.6H, TableS1). Co-expression of CD206 on hepatic CD163^{+} macrophages was confirmed by flow cytometry (Fig.S12E). These analyses indicate that cluster c3-Mφ-C1QA identified by scRNA-seq likely corresponds to the PD-L1^{+}CD163^{+} TAM cluster identified in CODEX.

Increasing frequencies of hepatic CD163^{+} Mφ with higher expression of PD-L1 and CD206 were found in HCC patients as compared to non-HCC patients (Fig.S12F–I). This indicates that presence of HCC in chronically diseased livers aggravates polarization of myeloid cells towards an immunosuppressive phenotype.

As the hepatic myeloid compartment between mice and humans shows considerable species-specific cellular (sub-)populations and gene expressions[35], we conducted additional single-cell RNA-seq analysis of CD45^{+} sorted leukocytes in tumor-free and HCC-bearing animals (Fig.6I-K). This additional dataset helped to confirm the presence of Mo/Mφ clusters c2_Mo/Mφ_Ftl1 and c4_Mo/Mφ_*Lyz2* that were expanded in tumor-bearing mice (Fig.S12J). Cluster c2_Mo/Mφ_Ftl1 showed characteristics of an immunosuppressive TAM phenotype and high expression of *Cd274, Mrc1* and *Arg1*. Analogous to the c3-Mφ-C1QA TAM cluster in human, tumor-associated Mφ in mice (Fig.6J&K) could be distinguished from dendritic cells through higher expression of *Csf1r* and *Lyz2* compared to other myeloid cells, e.g. c8_cDC and c9_pDC. We then tested these genes to target TAMs and test their interaction with MAITs in murine tumor models (Fig.7 and Fig.S13).

MAIT dysfunction in murine HCC can be reversed by PD-L1 blockade in vivo and by depletion of CSF1R$^+$ TAMs

As outlined above, we hypothesized that targeting CSF1 receptor expressing myeloid cells could be used to disrupt the TAM-MAIT cell inhibitory interaction. Our scRNA-seq data in human and mouse HCC samples indicate that CSF1R could be used to distinguish Mo/Mφ from dendritic cells. We thus aimed for a selective depletion of monocytes/macrophages (MMs) in mice. We used a transgenic mouse strain (MM^{DTR}) encoding for human diphtheria toxin receptor (DTR) that requires overlapping expression of *Lyz2* and *Csf1r*[36] allowing for the specific ablation of macrophages when DT is administered repeatedly. MM^{DTR} mice were used to assess the effect of MM depletion on MAIT cell phenotype in tumor-bearing mice. (Fig.7A). Flow cytometric analysis showed a specific depletion in the hepatic F4/80^{high}CD11b^{int} macrophage population, while conventional dendritic cells (defined as F4/80$^-$/CD11c^{high}MHC-II^{high}) remained unaffected (Fig.7B). Depletion of Mo/Mφ not only resulted in a significant increase in tumor infiltrating MAITs (Fig.7C), but also altered their phenotype, leading to a significant boost in IFNγ, TNFα and granzyme B expression (Fig.7D). Alternatively, we used anti-CSF1R antibodies to target CSF1R$^+$ myeloid cells in livers of tumor-bearing mice (Fig.S13A). A trend towards a higher absolute number and frequency of tumor-infiltrating MAITs was observed upon anti-CSF1R treatment (Fig.S13B) with a significant increase in the expression levels of pro-inflammatory IFNγ, TNFα and granzyme B (Fig.S13C). Therefore, CSF1R$^+$ TAMs in mice have a critical role in MAIT cell impairment and provide an immunosuppressive niche within the hepatic TiME.

To test if the MAIT cell impairment in HCC tumors depends on PD-1/PD-L1 interactions with TAMs in the adjacent liver, we next investigated whether immune checkpoint blockade targeting PD-L1 could restore MAIT cell function *in vivo*. RIL-175 (Fig.7E) or MC38 (Fig.S13D) tumor-bearing mice received anti-PD-L1 which resulted in a significant increase in MAIT cell infiltration into liver tumors (Figs.7F&G, Fig.S13E), indicating that MAIT cell migratory impairment was partly mediated through PD-L1 signaling. Higher infiltration of MAIT cells into hepatic tumors was accompanied by a significant increase in T_H1 transcription factor T-bet expression (Fig.S13F) and higher levels of IFNγ and granzyme B upon ICB treatment (Fig.7H, Fig.S13G). These findings indicate that the loss of T_H1/cytotoxic phenotype observed on MAIT cells was partly mediated through PD-1/PD-L1 signaling.

As PD-L1 is also expressed on the syngeneic tumor cells used in this study, we tested whether the dysfunctional phenotype of hepatic MAIT cells was mediated through PD-L1 on tumor cells. We generated Cd274$^{-/-}$ clones of Hep55.1c, B16-F10, RIL-175 and MC38 (Fig.S13H). Intrahepatic Hep55.1c tumor growth led to comparable MAIT cell phenotypic changes as measured by expression of surface markers PD-1 and LAG-3 in both WT and *Cd274*$^{-/-}$ clonal cell lines (Figs.S13 I&J), suggesting other mechanisms that impair MAIT cell dysfunction independent of PD-L1 expression on tumor cells.

The experimental data so far suggested a role of TAMs and PD-L1 in MAIT cell dysfunction. As our CODEX data (Fig.5F), flow cytometric analysis of patient samples (Fig.6E) as well as the scRNA-seq data derived from tumor-bearing mice (Fig.6K)

revealed high PD-L1 expression on TAMs, we knocked down PD-L1 in macrophages using two different approaches. We used *Lyz2*^{CRE} and *Csf1r*^{CRE} mouse strains to generate *Lyz2*^{CRE}*Cd274*$^{fl/fl}$ as well as *Csf1r*^{CRE}*Cd274*$^{fl/fl}$ *mouse* lines and tested the effect of each conditional knockout on MAIT cell phenotype in HCC-bearing mice (Fig.7J). Flow cytometry analysis confirmed that CD11b^{int}F4/80^{high} macrophage populations have higher expression of PD-L1 compared to F4/80^{-}CD11c^{high}MHC-II^{high} conventional dendritic cells in tumor-bearing livers (Fig.S13K), in line with our findings in human (Fig.5F, Fig.6E) and mouse scRNA-seq (Fig.6K). We confirmed reduced expression of PD-L1 on CD11b^{int}F4/80^{high} TAMs for both the *Lyz2*^{CRE}*Cd274*$^{fl/fl}$ as well as *Csf1r*^{CRE}*Cd274*$^{fl/fl}$ lines compared to *Cd274*$^{fl/fl}$ controls (Fig.S13L). PD-L1 expression was also reduced on CD11c^{high}MHC-II^{high} DCs in *Csf1r*^{CRE}*Cd274*$^{fl/fl}$ mice but not in *Lyz2*^{CRE}*Cd274*$^{fl/fl}$ mice (Fig.S13M). These experiments demonstrate that PD-L1 depletion on CSF1R^{+}TAMs result in an enhanced MAIT cell infiltration into orthotopic HCC tumors (Fig.7K) as well as improved cytotoxic function (Fig.7L)

Activated MAIT cells can synergize with aPD-L1 ICB to control orthotopic HCC in mice

Lastly, we investigated whether MAIT cells can contribute to aPD-L1 based immunotherapy for HCC. We recently developed a strategy to expand hepatic MAIT cells in mice using MAIT-ligand 5-OP-RU in combination with TLR-9 agonist CpG[12]. We combined this treatment with aPD-L1 (Fig.7M). As expected, 5-OP-RU/CpG treatment led to a robust expansion of hepatic MAIT cells in WT mice but not in *Mr1*$^{-/-}$ mice (Fig.S13N&O). Consequently, MAIT-cell activation in combination with aPD-L1 treatment reduced orthotopic HCC tumor growth in wildtype mice, but not in *Mr1*$^{-/-}$ mice (Fig.7N vs. O). These findings substantiate that anti-tumor polarized hepatic MAIT cells can contribute to successful aPD-L1-based immunotherapy of HCC in mice. Taken together, these experimental data indicate that the TAM-MAIT axis impairs MAIT cell function in HCC. Our data also suggest that MAIT cells are a target of aPD-1/aPD-L1 directed immunotherapy in HCC.

DISCUSSION

Collectively, our findings elucidate a critical role for MAITs in HCC and shed light on a MAIT-TAM crosstalk within the TME that drives hepatic MAIT cell dysfunction through PD-1/PD-L1 interaction in human and mice.

Consistent with previous reports in liver cancer[8,9,16,19], we found MAIT cell numbers to be reduced in the tumor core compared to the adjacent liver, a finding which was robustly obtained across the three assays, scRNA-seq, CODEX and flow cytometry. We have also demonstrated that hepatic MAIT cells in WT mice contribute to anti-tumor immunity, as MAIT-deficient *Mr1*$^{-/-}$ mice presented with higher tumor burden. These findings are in contrast with previous reports derived from mouse models of lung metastasis[10]. In this study, murine MAITs were found to exert tumor-promoting function through secretion of IL-17A induced by MR1 expression on tumor cells, eventually leading to a relative protection of *Mr1*$^{-/-}$ mice compared to WT mice. As the HCC tumor cell lines in our models did not express MR1 and the dysfunctional MAIT phenotype could also be observed using the

B16-*Mr1*$^{-/-}$ model[12], this mechanism does not apply to the setting described here and might partly explain, why different clinical and preclinical studies have associated MAITs with seemingly paradox outcomes. Our findings further substantiate the notion that the contribution of MAIT cells to tumor immunity is context-dependent, influenced by tumor intrinsic factors such as cancer type and stage, but also patient cohort, organ site and composition of the TiME.

ScRNA-seq of sorted MAIT cells revealed heterogeneity of MAIT cells in HCC. While recent scRNA-seq studies of leukocytes in HCC described the presence of MAITs within T cell clusters[13,14,16], little is known about MAIT cell heterogeneity. We found subclusters of MAIT cells that show clear signs of aberrant activation and late dysfunction, in line with previous reports[8,19 17]. Expression of immune checkpoint marker genes in two of the MAIT subclusters was accompanied by a loss of cytotoxicity that parallels dynamic changes in gene expression recently demonstrated for conventional CD8 T cells in HCC[14]. While reduced capacities of tumor-associated MAITs to produce pro-inflammatory cytokine/effector molecules has been described across different tumor entities[8,19,37], our scRNA-seq data sorted cells indicate that MAIT phenotypes are not binary states but rather reflect some functional plasticity.

Recent imaging-based analyses of the TiME have demonstrated the necessity to describe higher-order tissue architecture beyond just the numerical cellular composition to fully understand the continuum of tissue structure that eventually governs function[26,38]. We developed an image analysis pipeline in line with previous approaches[39]. We then analyzed the multicellular, spatially informed tissue signatures of the MAIT cell-niche in HCC. S^3-CIMA revealed the coordinated transitions between MAIT phenotypic states that were delineated based on the co-localization of neighboring PD-L1$^+$ TAMs in the adjacent liver. Interactions between MAITs and macrophages or monocytes has been proposed in the context of obesity-induced inflammation and fatty liver disease[40,41], infection[42,43] or vaccination[44]. While NK cells have been identified as key downstream interacting cells for MAITs in murine cancer models[10,11] and patient samples[11], cellular (immune) components that orchestrate MAIT cell function in cancer tissue have not been described. Our data-driven approach identified PD-L1$^+$CD163$^+$ TAMs enriched in the MAIT cellular neighborhood and showed that this interaction is located predominantly in the adjacent liver tissue.

We found high levels of PD-1 expression on MAIT-cells in the TiME which was further increased within the vicinity of the HCC tumor (Fig.5D)[8,19]. Recently, it has been reported that MAIT cell frequencies in PBMCs could be restored by ICB treatment in melanoma patients responding to treatment[45] and patients with high frequencies of circulating MAITs were more likely to respond to aPD-1 therapy with significantly improved overall survival in a second study[46]. The role of MAIT cells during ICB and whether these cells contribute to antitumor immunity or even mediate treatment failure is unclear.

This work shows that MAIT antitumor immunity and response to ICB therapies relies on organized, spatially nuanced interactions between MAITs and PD-L1$^+$CSF1R$^+$ TAMs within the tumor immune microenvironment (TiME). Thus, targeting the MAIT–TAM axis could

help to fully capitalize on the unique capabilities of MAIT cells within the TiME and help design new therapeutic combinations in HCC.

LIMITATIONS OF THE STUDY

The sample size of the patient cohort used in this study is relatively modest and samples were procured from a single medical center. Stratification of HCC patients according to survival or recurrence was not possible as such data was not available at the time of submission. Further prospectively collected clinical and experimental data from HCC models with progressive outgrowth are needed to investigate how dysfunctional MAIT cells and their impaired infiltration of HCC lesions is a prevailing factor in tumor initiation and progression. Low MAIT cell counts in murine livers compared to human represent a major challenge in dissecting contribution to anti-tumor immunity in mouse models of ICI. A larger patient cohort should also be investigated to assess the contribution of MAIT cell changes in HCC patients in response to immune checkpoint therapy. The current patient ICI cohort with available pre- and post-therapy liver biopsies is limited by low MAIT cell numbers in the dataset.

STAR METHODS

Lead contact

Further information and requests for resources and reagents should be directed to the lead contact Tim F. Greten (tim.greten@nih.gov).

Resource availability

All unique reagents generated in this study will be available from the lead contact upon request.

Data and code availability

The single-cell RNA sequencing (scRNA-seq) as final QC-filtered data for analysis and raw CODEX imaging data generated from this study are available through NCI Cancer Research Data Commons (*CRDC*).

The human single-cell sequencing data are deposited through dbGaP (accession number: phs003279.v1.p1).

The murine scRNA-seq data can be accessed through GEO (accession number: GSE231712).

The raw CODEX images are hosted at The Cancer Imaging Archives (TCIA) under https://doi.org/10.7937/bh0r-y074.

This paper also analyzes existing, publicly available data. These accession numbers for the datasets are listed in the key resources table.

All original code used to analyze CODEX images including S^3-CIMA as well as the scRNA-seq analysis pipeline has been deposited at https://github.com/claassenlab/S3-CIMA and is described in detail in Babaei et al.[29].

Some figures were created with http://biorender.com/.

Any additional information required to reanalyze the data reported in this paper is available from the lead author upon request.

EXPERIMENTAL MODEL AND SUBJECT DETAILS

Human HCC specimens

Discovery cohort: We decided to study potential MAIT cell heterogeneity and their cellular interactions in the TiME of HCC. We performed a comprehensive analysis on prospectively collected, surgically removed tumor specimens, and paired adjacent non-tumor liver tissue from n=15 individuals undergoing HCC resection using highly multiplexed CODEX tissue imaging of whole tissue sections, single-cell RNA sequencing and high dimensional flow cytometry (see study designs, Fig. S1). A total of 37 patients with pathologically confirmed HCC treated at the MedStar Georgetown University Hospital (GUH) in Washington D.C. were enrolled in this study. Detailed clinical and pathological information is shown in Table S1. An additional non-HCC patient cohort (n=23) was prospectively enrolled from patients with chronic liver disease requiring liver transplantation or hepatic resection outside of the HCC-context. Collection and processing of human HCC specimen has previously been described[47]. HCC specimen from patients undergoing surgical HCC resection (patient samples for flow cytometry, scRNA-seq and CODEX) or orthotopic liver transplantation (some patients in the extended cohort for flow cytometry) at MedStar Georgetown University Hospital were collected. All patients gave informed consent for collection of clinical information, tissue acquisition under the Institutional Review Board (IRB)-approved protocol IRB #2017-0365 and the material transfer agreement (M.T.A.#43655-18) between the GUH and the U.S. National Cancer Institute (NCI).

Validation cohort (ICB cohort): We recently described[34] collection of pre- and post-treatment biopsy specimen with preoperative informed consent from patients participating at NIH Clinical Center for interventional studies, following approval by the ethics committee of the National Institutes of Health (ClinicalTrials.gov Identifier: NCT01313442). A total of 8 HCC patients were identified with single-cell RNA-seq data available for pre- and post ICB treatment.

Animal models: Mice were housed at CRC animal facility at NCI in accordance with the National Research Council Guide for the Care and Use of Laboratory Animals. All technical procedures and experimental endpoints were approved by the NCI Division of Intramural Research Animal Care and Use Committee and listed in the animal study proposals MOB-028 & TGOB-013.

Two-to-four months-old male and female C57BL/6 (strain code #556) mice were purchased from Charles River Laboratories. *Mr1*$^{-/-}$ mice were generated and described[5] by Dr. Susan Gilfillan (Washington University, St Louis School of Medicine, MO) and were kindly

provided by Dr. Daniel Barber (NIAID/NIH, Bethesda, MD). Male and female *Mr1*$^{-/-}$ mice between 8–16 weeks of age were used for the experiments. Loss of MR1 was confirmed by genotyping of *Mr1*$^{-/-}$ mice using PCR with the following primers: MR1 5 8763–8783: AGC TGA AGT CTT TCC AGA TCG, MR1 9188−9168 rev: ACA GTC ACA CCT GAG TGG TTG, MR1 10451−1043: GAT TCT GTG AAC CCT TGC TTC. *Lyz2*^{Cre} *x* *Csf1r*$^{LsL\text{-}DTR}$ (MM^{DTR}) mice have previously been described[36]. This transgenic mouse strain utilizes a two-gene approach (targeting *Lyz2* and *Csf1r* double-positive cells) that allows for toxin receptor–mediated conditional cell ablation of monocytes, macrophages, and inflammatory monocytes, while conventional splenic dendritic cell (cDCs) and lymphocytes are unaffected. The *Lyz2*^{Cre} mice (strain #004781) and *CSF1r*$^{LsL\text{-}DTR}$ mice (strain #024046), *CSF1r*$^{LsL\text{-}DTR}$ mice (strain #024046), Csf1r^{Cre} (stain#: 029206), and Cd274$^{fl/fl}$ (strain #: 036255) were purchased from Jackson Laboratory and housed in NCI CRC facility. *Lyz2*^{Cre} mice were crossed with *Csf1r*$^{LsL\text{-}DTR}$ mice to generate *Lyz2*^{Cre} x *Csf1r*$^{LsL\text{-}DTR}$ (MM^{DTR}) mice. *Lyz2*^{Cre}*Cd274*$^{fl/fl}$ as well as *Csf1r*^{Cre}*Cd274*$^{fl/fl}$ were generated through crossings of *Cd274*$^{fl/fl}$ line with *Lyz2*^{Cre} or *Csf1r*^{Cre} respectively. Mice were genotyped through service provided by TransnetYX. Synthesis and application of riboflavin pathway derived MAIT cell antigen 5-OP-RU in combination with Class B CpG Oligonucleotide (ODN 1826, Invivogen, San Diego, CA) has previously been described[12,48.]

Cell lines: The luciferase-expressing HCC cell line RIL-175 has previously been described[49] and was cultured in RPMI 1640 GlutaMax (ThermoFisher, Cat No. 61870127) +10% FCS (CORNING, Cat. no. MT35010CV). Syngeneic HCC cell line Hep55.1c was purchased from CLS Cell Lines Service GmbH, Germany (Cat. No. 400201). The B16-F10 *Mr1*^{WT} as well as targeted knockout of *Mr1* in B16F10-GFP+LUC cells using CRISPR/Cas9-mediated gene editing has previously been described[12]. Loss of MR1 protein surface expression in monoclonal B16F10-*Mr1*$^{-/-}$ was confirmed by flow cytometry after ligand stimulation with 5-OP-RU. Cells were cultured in RPMI1640 GlutaMax (+10% FCS) + 1% So-Pyruvate (Thermofisher, Cat. No. 11360070) +1% 1M HEPES (Thermofisher, Cat. No. 15630080) +1% NEAA (Thermofisher, Cat. No. 11140050) and 500 ng/mL Puromycin (InvivoGen, Cat. No. ant-pr-1). Colorectal cancer cell line, MC38 (RRID: CVCL_B288) was a gift from Dr. Jay Berzofsky at the U.S. National Cancer Institute.

All cell lines used in experiments were cultured for 3 to 7 days and maintained at 37°C with 5% CO_2 for 1 to 3 passages prior to implantation. Routine testing for murine pathogens including Mycoplasma was last performed in March 2019 and was negative for all cell lines.

METHOD DETAILS

Human tissue processing—Paired adjacent liver (> 2cm away from tumor tissue) tissue, margin (rim) and tumor core tissue were collected from surgically removed specimens and processed separately to generate single-cell suspensions (see study design, Fig. S1). For CODEX multiplex immunofluorescence imaging, a freshly obtained piece of the tumor-to-liver border from the same patient sample was cut and immediately embedded in optimal cutting temperature (O.C.T.) compound (FisherScientific, Cat. No. 23–730–571). Fast freezing was achieved by submerging the tissue in 2-methylbutane (FisherScientific, Cat. No. AC167840010) which was cooled down on dry ice. 10 μm thick tissue sections

were cut onto poly-Lysine coated glass cover slips. Coverslips (Electron Microscopy Sciences, Cat. No. 72204–01) were manually coated with 0.1% poly-L-lysine solution (Sigma-Aldrich Cat No. p8920) for 24 hrs followed by 6 x washes in diH2O and drying. The coverslips were used for no longer than 2 months after coating.

Single cell isolation from surgical specimen—Fresh tissue was collected in the operation room and immediately immersed in MACS tissue storage solution (Miltenyi Biotec, Cat. No 130–100–008) and transported to the lab on ice. Tissue blocks were manually minced into smaller pieces using a sterile razor blade. The tissue was then digested in serum-free RPMI 1640 (ThermoFisher, Cat. No. 61870127) containing collagenase IV (activity approx. 300 CDU/10ml, STEMCELL technologies Cat. No 07909) and DNAse I (activity approx. 300 Kunitz/10ml, STEMCELL Technologies Cat. No. 07900) shaking for 90 minutes at 37°C. Washing and filtering was then followed by a density gradient centrifugation using 40% and 80% Percoll PLUS solution (in PBS; GE Healthcare, Cat. No. GE17–5445–01) to separate the mononuclear immune cells from the parenchymal cells. Centrifugation was performed at 2400 RPM, for 20 min at RT without brake. Immune cells were collected from the interface layer and washed with RPMI once. RBC lysis (ThermoFisher, Cat. No. 50–112–9751) was performed before cells were counted. Cells were then used for immediate flow cytometry analysis or cryopreserved. For cryopreservation, mononuclear cells were resuspended in Recovery™ Cell Culture Freezing Medium (Gibco, Cat. No. 12648010), transferred into cryotubes and then stored at −80°C.

Single cell sorting—The cryopreserved immune cell suspension was thawed at 37°C for rapid recovery and washed with FACS buffer (BD, Cat. No. 554656). Cell count and viability were assessed on a CellometerAuto200 (Nexcelom Bioscience).

Fixable Viability dye ZOMBIE-UV (Biolegend, Cat. No. 423108) was applied to cell suspensions for 20 min at 4 °C. After Fc-blocking (BD, Cat. No. 564220) for 15 minutes at 4°C, surface staining including tetramers was performed by incubating 1–2 × 10^6 cells at 4°C for 30 min in staining buffer (BD Bioscience, catalogue no. 554656). The following antibodies were used for FACS sorting: CD45 (Biolegend, Cat #: 304023), CD14 (BD, Cat #: 561391), CD15 (BD, Cat #: 561585), CD19 (BD, Cat #: 561125), CD3 (Biolegend, Cat #: 300430), CD161 (Biolegend, Cat #: 339918) & hMR1 tetramer loaded with 5-OP-RU (NIH tetramer core facility). To enrich for MNCs and to purify MAIT cells respectively, live $CD45^+$ MNCs or MAIT cells (defined as live lymphocytes, $CD45^+CD14^-CD15^-CD19^-CD3^+CD161^+$MR1-tetramer/5-OP-$RU^+$ see Fig. S3A for gating strategy) were sorted on a BD Influx (BD) into sterile PBS. Next, sorted cells were instantly transferred for single-cell cell capture and library preparation.

Single Cell – Partitioning and library preparation—Single cell suspensions after FACS sorting were washed once with ice-cold PBS with 0.04% BSA by centrifugation at 300g and gently resuspended in fresh buffer. Cell counts and viability measurement were taken of each cell suspension using a fluorescent cell counter and propidium iodide and acridine orange dyes (LunaFL, Logos Biosystem). Cell concentrations were adjusted and loaded onto the 10x Genomics Chromium platform using the 5’ v1.1 immune profiling chemistry (10x Genomics) targeting 6,000 cells when sample amounts and viabilities

allowed. For samples where available number of cells was low, additional washes were skipped and cell counts were based on flow sorting event counts. Preparation of gene expression scRNA-Seq and associated human TCR enrichment libraries were performed according to vendor recommendations.

Single Cell – Sequencing—Sequencing was performed on either the Illumina NextSeq 550 or Illumina NextSeq 2000 instrument. For scRNA-Seq gene expression, libraries were sequenced with a 26bp read to identify cell barcodes and unique molecular indices, an 8bp read for sample indices, and a 91–98bp read to identify cDNA insert. For single cell TCR sequencing, libraries were sequenced with paired end 150bp reads to increase VDJ coverage, and an 8bp read for sample indices. Samples were multiplexed for sequencing based on library type and sample groups, and reads were combined from multiple sequencing runs to achieve at least 50,000 reads per cell on average for gene expression and at least 5,000 reads per cell for TCR libraries for all samples.

Single Cell – Data processing—Data was processed using the 10x Genomics Cell Ranger pipeline (v4.0, v5.0 or v6.0) to demultiplex reads and then align reads to a GRCh38 reference (refdata-gex-GRCH38–2020-A) for scRNA-Seq data and a GRCh38 VDJ reference for single cell TCR data (refdata-cellranger-vdj-GRCh38-alts-ensembl−5.0.0). UMI-adjusted aligned reads were used to generate a single cell barcode and gene expression matrix and a TCR clonotype matrix that was used for downstream analysis.

Unsupervised clustering of scRNA-seq data and cell type definition—The scRNA-seq data was analyzed using the Scanpy library (version 1.9.1 (Wolf et al., 2018)) using read counts matrices. Preprocessing, quality control (QC), and clustering were performed separately for all $CD45^+$ and selected/sorted MAIT cells. To remove possible doublets, *Scrublet* (Wolock et al., 2019) was applied per sample. The doublet threshold per sample was chosen to match the expected number of multiplets according to resources tables provided by 10X genomics (https://kb.10xgenomics.com/hc/en-us/articles/360001378811-What-is-the-maximum-number-of-cells-that-can-be-profiled). Outlier removal based on mean absolute deviation around the median was applied. For the measures, log1p_total_counts, log1p_n_genes_by_counts, and pct_counts_in_top_50_genes cells were marked as an outlier in case, they exceeded a threshold of five MADs. QC consisted of removing genes expressed in too few cells and cells expressing too few genes. More specifically, a threshold of min_genes=200 and min_cells=20 was applied. Furthermore, cells were only included if mitochondrial, ribosomal, and hemoglobin gene read count fractions were below thresholds of <3%, >15%, and <0.2%, respectively. Mitochondrial, ribosomal, and hemoglobin genes and MALAT1 were removed for further analysis. After stringent quality control, a total of n= 44,454 cells were used for the analysis (3,663– 8,481 cells/patient; median: 4,795.5cells/patient). Genes with >3000 total counts across the dataset were removed. Counts per cell were normalized to 10,000 reads per cell. Read counts were transformed with log(x+1). For further analysis, only highly variable genes were considered. These genes were selected using the function highly_variable_genes with default parameters. Batch effect correction across patient samples was performed using the *Harmony* algorithm[50] to patient labels. The neighborhood graph was built using the

function neighbors with parameters n_neighbors=30 and n_pcs=20. The resulting data was clustered with the *Leiden* algorithm[51]. For final annotations, resolution=1.0 was used.

For a subset of n=6 patients, MAIT cells were FACS sorted using MR1 tetramers loaded with 5-OP-RU (Fig. S1A) and subjected to scRNA-seq and TCR seq as described above: four matched adjacent liver and tumor core (LHCC44, LHCC45, LHCC48, LHCC54) and one each for adjacent liver (LHCC40) and tumor core (LHCC47). Using MR1 tetramers loaded with 5-OP-RU, a total of 46,588 MAIT cells were sorted at a >95% purity (Fig.S2A). To further investigate cellular heterogeneity among the MAIT cell population, MAIT cells from $CD45^+$ sorted leukocytes (Fig.1A, Fig.S2A) and FACS sorted MAIT cells (Fig.S2A) were captured, sequenced, and analyzed together with FACS purified MAIT cells. MAIT cells among total $CD45^+$ cells were identified by TCR sequencing in line with Yao et al.[15]. After processing of TCR-seq data as described above, this allowed for the identification of T cells expressing transcripts for the canonical MAIT TCR alpha chain. Cells with detectable *TRAV1–2* transcript that had productive combination with either *TRAJ33, TRAJ12* or *TRAJ20* were defined as MAIT cells.. Next, QC was performed as described above with the following settings: For mitochondrial, ribosomal, and hemoglobin gene read count thresholds of <5%, >20%, and <0.01% were used, respectively. Genes with >3000 total read counts were removed. For *Leiden* clustering-based final annotations, resolution=0.4 was used. After QC and downsampling, a total of 7,763 MAIT cells from 8 patient samples were then used for downstream analysis. A maximum of 1,000 MAIT cells per sample was selected to ensure a balanced representation of each patient sample and to ensure that the conclusions reached about MAIT cell heterogeneity would not be driven by patient-specific effects.

Differentially expressed gene analysis for hepatic and tumor infiltrating leukocytes—For both the $CD45^+$ sorted and MAIT sorted cells, differential gene expression analysis was done by using the rank_genes_groups function of Scanpy with use_raw=True and method='wilcoxon'.

Validation cohort ([16])—An independent patient cohort with available single-cell RNA sequencing data data published by Zheng *et al.*, 2017 was re-analyzed to validate the findings from the MAIT analysis. The dataset consists sorted T cells including one MAIT-dominant cell cluster (C03_CD8-SLC4A10). A similar analysis matching the aforementioned steps for MAIT-sorted cells was conducted. The neighborhood graph was calculated using n_neighbors=30 and n_pcs=20. Leiden clustering algorithm with resolution=0.8 was used to subcluster MAIT cells were subclustered. The pairwise Pearson correlation between all clusters from both MAIT cell cohorts was calculated for qualitative comparison by considering the top 25 genes from the shared differentially expressed genes.

MAIT cell transcriptomic profile in patients treated with ICB—Patient characteristics, sample acquisition and scRNA-seq data processing for liver cancer patients treated with ICB have previously been described[34]. Briefly, tumor tissue biopsies before and after treatment initiation for n=8 patients with HCC undergoing ICB were available for analysis. These core needle biopsies were subjected to scRNA-sequencing (Fig. S12G). MAIT cells were identified in scRNA-seq data by re-clustering of T cells using *Leiden*

algorithm[52] based on shared nearest neighbors. Specifically, Seurat's *FindNeighbors* and *FindClusters* algorithms with parameters of the first 10 principal components and a 1.5 resolution were used. Next, we performed differential gene expression analysis for each cluster. The cluster of MAIT cells could be determined based on MAIT cell marker genes such as *SLC4A10, KLRB1, NCR3, and ZBTB16* (TableS1). The cytotoxicity score was determined as the average expression for proinflammatory/cytotoxic genes *IFNG, GZMA, GZMB, GZMH, GZMK, GZMM, GNLY, PRF1, KLRC1, KLRB1, NKG7, KLRK1, KLRD1, FASLG, TNF, IL2* per MAIT cell.

Survival analysis—We tested the significance of a published MAIT cell signature (SLC4A10, KLRB1, ME1, TMIGD2, IL23R, NCR3, LST1, COLQ, RORC, ZBTB16, TLE1)[15] and the MAIT cell signature derived from cluster c9_MAITs (with a cutoff LogFc=1.5) on patient outcome by using several published bulk transcriptomic datasets derived from HCC tumor samples. Transcriptomic data of 371 patients diagnosed with HCC are accessible through the The Cancer Genome Atlas Program (TCGA, https://cancergenome.nih.gov/) LIHC cohort, with data on overall survival (OS) available for 364 patients. The LCI[53] and TIGER-LC[54] HCC patient cohorts have previously been published and can be accessed through GEO under the accession numbers GSE76297 and GSE14520. R survival and *survminer* packages were applied for survival analysis. Samples were divided into two equal-sized groups based on the median value of the MAIT signature. Kaplan-Meier method was applied to calculate the survival probability. Statistical significance was tested using a log-rank test.

Co-detection by indexing (CODEX) multiplexed tissue imaging of 38 markers in fresh frozen tissues of 15 HCC patients

Screening and validation of CODEX antibodies: Some antibodies in our 37-plex CODEX panel were commercially available, already conjugated to oligonucleotides and ready to use through Akoya biosciences or Leinco technologies (see Table S1). We re-conjugated some of these commercially available, CODEX validated antibodies to different oligonucleotide tags. Beyond that, we developed 21 different antibodies for CODEX imaging with the intention to identify all major cell types in human liver cancer with a focus on (lymphoid) immune cells. Each developed CODEX antibody was screened, titrated, and validated in manual single- or dual-color conventional immunofluorescence imaging on non-HCC fresh frozen liver tissue (Fig.S5). The staining for each clone was assessed before and after conjugation to the CODEX oligonucleotide tags. Performance of each developed clone was assessed through CODEX imaging of both liver and secondary lymphoid organs (spleen or lymphnode) using the full 37-plex antibody panel. For conventional IF, the tissue was thawed and fixed in acetone (Macron Chemicals, Cat.No. MK244310) followed by rehydration with commercial hydration buffer (Akoya Biosciences, Cat.No 7000008 Part Number 232105) and another fixation step in 1.6% paraformaldehyde (Thermo Scientific Cat.No 28908). After blocking with Staining solution (Akoya Biosciences, Cat.No 7000008 Part Number 232106) primary antibody staining was performed for 3 hrs at RT. Counterstaining with HOECHST (ThermoFischer, Cat.No H3570) and fluorophore-coupled secondary antibodies was achieved by incubation for 30 min at RT. Staining patterns

were confirmed with online resources (The Human Protein Atlas, Pathology Outlines) and published literature.

Antibody-conjugation with oligonucleotide-tags: Carrier free antibodies were conjugated to selected barcodes using commercial reagents following Akoya Bioscience's recommended protocols. First, preservatives and other additives (like trehalose) were removed by using Amicon Ultra 30K centrifugation filters (Millipore, Cat. No. UFC503024). The filters were hydrated with PBS for 5 min followed by centrifugation at 5,000 x g for 4 min on a tabletop centrifuge (Eppendorf 5424). The filter was washed once more with 400 ul PBS. After the remaining buffer was removed from the filter, 70 ug antibody was added in a final volume of 300 microliters in PBS, followed by centrifugation at 5,000 x g for 4 min. The antibody was washed two more times with 400 ul PBS. After the second centrifugation 80–100 ul antibody was left in the filter and transferred to a new tube. The protein concentration was measured using an Implen nanophotometer with IgG mouse settings. 3 ul of antibody solution was set aside for conjugation quality control. 50 ug of protein was used for conjugation, diluted in 100 ul PBS.

For conjugation, Amicon Ultra 50K centrifugation filters (Millipore, Cat. No. UFC505024) (one for each conjugation) were washed with 500 ul filter blocking solution (Akoya Biosciences, Cat. No. 7000009 Part No 232113) and centrifuged at 12,000 x g for 2 min. The remaining solution was discarded and 50 ug antibody in a volume of 100 ul supplemented with PBS was added to the filter followed by centrifugation at 12,000 x g for 8 min. 260 ul antibody reduction master mix (Akoya Biosciences, Cat. No. 7000009 Part No. 232114 and Part No.232115) was added to the filter and incubated for 30 min. After centrifugation at 12,000 x g for 8 min, the filter was washed with 450 ul of conjugation buffer (Akoya Biosciences, Cat. No. 7000009 Part No. 232116). The barcode was resuspended in 10 ul nuclease free water (Ambion AM9938) and complemented with 210 ul of conjugation buffer. The mix was added to the filter and incubated for 2 hours. 7 ul of the mix was set aside for testing the conjugation efficiency and the filter was centrifuged at 12,000 x g for 8 min. Next the conjugated antibody on the filter was washed three times with 450 ul purification solution (Akoya Biosciences, Cat. No. 7000009 Part No. 232117) and resuspended into 100 ul of antibody storage solution (Akoya Biosciences, Cat. No. 7000009 Part No. 232118). The antibody was collected by inverting the filter and centrifuging the content into a new tube at 3000 x g for 2 min. The collected conjugated antibody was stored at 4°C.

Validation of antibody – oligonucleotide conjugation: The unconjugated (3 ul) and conjugated (7 ul) antibody aliquots previously set aside were diluted to 10 ul with PBS. After addition of 10 ul of 2X Laemmli buffer (BioRad Cat. No. 161–0737), the samples were denatured at 100°C for 8 min and loaded onto 4–20% Novex Tris-Glycine gels (Invitrogen, Cat. No. XP04200BOX) for electrophoresis at 150 V for 2 hrs. After electrophoresis the gel was rinsed 3 times for 5 min in diH2O and stained with InstantBlue Coomassie-based Staining solution (Expedeon Protein Solutions, cat. No. ISB1L) overnight to visualize the protein bands. The gels were rinsed in diH2O to remove the background and imaged using a BioRad Chemidoc imaging system.

Staining procedure of fresh frozen tissue sections for CODEX imaging: Tissues sectioned onto poly-L-lysine coated coverslips were kept at −80°C until stained for CODEX imaging. The tissue fixation and staining steps were performed following the recommended protocol from Akoya Biosciences using commercial staining reagents (Akoya Biosciences Cat. No. 7000008). The staining steps were performed in 6 well plates or humidified staining chamber.

The tissue was fixed for 5 min in acetone (Macron Chemicals, Cat.No. MK244310), air dried for 2 min followed by hydration 2 × 2 min in hydration buffer (Akoya Biosciences Cat. No. 7000008 Part No. 232105). The tissue was fixed for 10 min in 1.6% paraformaldehyde diluted in hydration buffer and kept in staining buffer for no more than 30 min before staining. Staining was done in staining buffer supplemented with Blocker N, blocker J, blocker S and blocker G (dilution factor 1:42) (Akoya Biosciences Cat. No. 7000008). Antibodies were combined at the dilutions indicated in Table S1. The tissue was stained at RT for 3 hrs followed by 2 × 2 min wash in staining buffer, followed by fixation in 1.6% paraformaldehyde diluted in storage buffer (Akoya Biosciences Cat. No. 7000008 Part No. 232106). The tissue was rinsed 3 X in PBS and fixed in ice cold methanol for 5 min. After rinsing in PBS for 3 times, the fixative (Akoya Biosciences Cat. No. 7000008 Part No. 232107) diluted in PBS was applied for 20 min followed by rinsing in PBS. The stained sample was kept at 4°C in storage buffer for less than two weeks or imaged immediately.

Whole slide multispectral imaging using CODEX multi-cycle reaction (level 1 data): While scanning small tissue regions (e.g. tissue microarrays, TMAs) allows for imaging a high number of patient samples, intra-patient heterogeneity of different cell populations within large tissue sections can be greater than true interpatient variability[27,55]. Imaging of stained slides was performed on BZ-X810 microscope using DAPI, FITC, CY3 and CY5 filters with a Keyence 20X objective with NA of 0.75 following recommendation from Akoya Biosciences. The number of tiles was selected to cover the area of the tissue and varied between 15 and 27. Multiple layers (Z-stack n=9–14), separated by 1.5 um, were acquired to make sure every cell in the tissue is in focus. A total of 12,703,216 microscopy images (tiles) were acquired. Imaging was done in multiple cycles using exposure times listed in Table S1. Total imaging time was 1,738 hours (~72 days).

Primary image processing (level 2 data): The images were transferred to the processing computer and processed using CODEX processor version 1.7.0.6 without segmentation. Nuclear staining from cycle 2 was used as reference for focusing. During processing background subtraction, deconvolution, best focus selection (EDF), shading correction were selected. After conversion, individual stitched tiff images were converted to pyramidal tiff using *bftools* open-source conversion tool (hosted on the NCI HALO infrastructure). Pyramidal tiff images were loaded into HALO and fused to create composite images for analysis.

Primary image analysis using HALO digital pathology software (Level 3 and level 4 data): Full resolution, high quality mosaic images (after stitching, registration, alignment, illumination correction & background subtraction) for each of the 38 markers (37 protein targets + nuclear stain DAPI) per patient sample were imported into HALO image analysis

platform (V3.2, Indica Labs; available through the NCI HALO Image Analysis Resource) and fused into a single multi-layer AFI file in HALO. Intensity adjustment for each marker in each tissue was done in HALO. High magnification, multi-color overlay images of CODEX datasets were exported through the figure maker function in HALO. Lower magnification, full-resolution multi-color overlay images were generated in ImageJ (Fiji version 2.8.5).

Tissue annotation: The whole tissue was masked (versus the background glass slide) using the classifier module in HALO which is based on a random forests machine learning algorithm. Areas of low tissue quality and regions with high autofluorescence such as folds, dried edges, bubbles, and necrotic tissue were excluded. The tumor region of the tissue was identified by an expert in liver cancer histopathology (D.K.) on H&E stained sections of adjacent frozen tissue. Tissue regions (adjacent liver, rim & tumor core) were then manually annotated within the HALO software for all cases accordingly, guided by the following markers: DAPI, HNF4α, CD34, LYVE-1, αSMA, Ki-67, panCK, EpCAM.

Cell segmentation: The HALO HighPlex FL module v3.2.2 module was used for cell segmentation and manual phenotyping. Cell segmentation was performed using DAPI-controlled watershed nuclear segmentation algorithm implemented in HALO. Digital overlays of the cell-segmentation masks were used to visually control the performance of single cell detection.

Manual gating: For manual gating of cell types, marker positivity of each marker was assessed visually, and positivity thresholds were set for each individual marker for each individual tissue section. This results in the classification of each cell as either positive or negative for the respective marker. Using a combination of canonical immune cell markers (in analogy to traditional gating e.g. in flow cytometry) the numbers and frequencies of major immune cell types were determined by manual gating for each tissue section and summary statistics were used for further analysis.

Numerical output: the HALO platform allows numerical data to be generated based on cell segmentation and provides spatial feature tables that include marker intensities, cell coordinates and other single-cell features like manual gating results or results of the tissue annotation (in analogy to count tables in scRNA sequencing). These CSV files containing single-cell data can then be used for further downstream analysis.

Unsupervised clustering analysis and cell annotation in CODEX data: The raw single-cell CODEX dataset consists of 4,567,421 cells derived from 15 HCC samples (Table S1). Intensity levels from 37 protein markers and nuclear dye DAPI were included in the following/downstream analysis. An arcsinh transformation was applied on raw intensity values for normalization. The cofactor was selected per patient and per marker for optimal performance of downstream clustering. Harmony was used on the patient label to account for batch effects[50]. For improved computation time, a GPU implementation (*harmony-pytorch* (v.0.1.6)) of the algorithm was used. Following this correction, a MinMax-transformation was applied to scale the marker expression level to the closed interval [0, 1]. Cell type annotation was achieved by first clustering the preprocessed data

using the *Leiden* algorithm for community detection[51,52] based on all protein markers. The clustering was implemented using the *RAPIDS* library[56] (version 0.18.0). Different kNN-graphs and values for the resolution parameter were considered. Each run was manually evaluated based on its distinctness of clusters. Annotation of clusters and assignment of corresponding cell types was guided by average marker expression of each cluster. The resolution parameter was chosen to result in an over-clustering, i.e. to produce more clusters than (expected) cell types. Using this approach, it was possible to map several clusters to the same cell type using domain knowledge and to achieve a final clustering guided by expert knowledge. The final kNN-graph was built with k=30 using cosine distance. Hereby, the clustering was done with resolution=2.2. For each cluster, cell annotation was manually verified by tracing single cells in each cluster based on unique cellular IDs as well as X/Y-coordinates onto the stitched images in HALO software. A total of 17,398 cells corresponded to artifacts and were removed. A more granular identification of immune cell types was achieved by separate clustering of $CD45^+$ cells based on manual HALO gating. This resulted in a subset of 1,485,139 immune cells that were used for downstream analysis. For leukocyte clustering, a subset of immune cell-specific markers (Fig.4D) was selected. The same clustering approach as for the complete dataset was applied. The selected result was obtained by using k=30 neighbors for the graph and a resolution value of 2.2. Following the same approach as outlined above, another 73,033 cells were found to be derived from artifacts or were classified as non-immune cells based on the microscopy images and, thus, excluded.

Spatial cell subset enrichment detection with S^3-CIMA[29]: The S^3-CIMA model has been applied as described previously[29]. Briefly, S^3-CIMA identifies cell subsets in cellular neighborhoods that are enriched with respect to a phenotype, such as tissue type. The model uses as input cell profiles of spatial nearest neighbors around MAIT cells as anchor. Cell profiles were obtained from arcsinh transformed and HARMONY normalized intensities of all 38 markers of the CODEX imaging data. K nearest-neighbors of each anchor cell ($10 \leq k \leq 100$) were calculated based on the Euclidean distance between an anchor cell and all cells in a specific tissue category per patient. Each input is labeled according to the corresponding tissue category as the phenotype. S^3-CIMA implements a weakly supervised classifier to identify cell subsets whose frequency distinguish the considered phenotypes. A set of randomly selected k nearest neighbor cells was included as a background phenotype. The number of background sets was set equal to the number of anchored inputs. To reduce bias in the classification model, multi-cell inputs of the patients with the high number of anchor cells is downsampled to the 90th percentile of the overall input sets. The inputs of eight (out of 15) patients were randomly split into training and validation sets (80% and 20% respectively). Controlling for variation due to the random selection of training and test sets, we repeated this approach with different seeds and noted that the classification accuracy did not differ significantly when swapping the test and the training dataset, indicating the robustness of the analysis. Then, 200 models were trained and the model with highest predictive accuracy on the validation set was selected. The remaining seven patients were used as the test set to assess the performance of the best model. The resulting model defines a score to rank and map the enriched cell subsets[29]. We selected and performed downstream analyses for the 5% top scoring cells. The relative frequency of selected cell of all input cells

per patient in each tissue type as well as background were calculated and compared using a Wilcoxon rank-sum test. We assessed the performance of this procedure using different k-nearest neighborhoods ($10 \leq k \leq 100$). The best neighborhood size was chosen at $k = 40$ achieving the highest frequency of selected cell significance.

Characterization of spatially enriched cell subsets—Enriched cell subsets possibly cover multiple cell types. We assessed how enriched cell subsets map to the annotated cell types, and how these are enriched across the considered conditions, i.e., tissue regions. To find spatially enriched cell subsets, an analytical enrichment score (ES) was calculated for each cell type per tissue type across all patients. Briefly, the enrichment score of each cell type was calculated based on the ratio of two factors, i) frequency of the cell type with high filter response in the anchor neighborhood (i.e., selected cells) and ii) frequency of the cell type with high filter response but not in the anchor neighborhood (Fig. S8A). The enrichment score of a specific cell type across the patient cohort is reported as the median value of the scores across all patients. The error bars are calculated as the median absolute deviation. A cell type was excluded if it was selected in less than 7 patients or the ratio of selected cell to all cell in the anchor neighborhood was less than 2%. Enrichment score values ES>1 indicates enrichment of the corresponding cell type in the spatial neighborhood of the anchor cell.

The enrichment score was calculated according to the following formulas:

Enrichment score:

$$\mathrm{ES}_{CT} = \frac{\mathrm{S}^{S}_{CT}}{\mathrm{S}_{CT}}$$

Score of cell type CT in nearest neighbor of the anchor cell is selected:

$$\mathrm{S}^{S}_{CT} = \frac{\mathscr{K}nn^{S}_{CT}}{\mathrm{E}^{S}_{CT}}$$

Score of cell type CT is in nearest neighbor of the anchor cell:

$$\mathrm{S}_{CT} = \frac{\mathscr{K}nn_{CT}}{\mathrm{E}_{CT}}$$

Expected value of CT in nearest neighbor of the anchor cell is selected:

$$\mathrm{E}^{S}_{CT} = \mathscr{K}nn^{S} \times \frac{\mathscr{K}^{S}_{CT}}{\mathscr{K}^{S}}$$

Expected value of cell type CT is in nearest neighbor of the anchor cell:

$$\mathrm{E}_{CT} = \mathscr{K}nn \times \frac{\mathscr{K}_{CT}}{\mathscr{K}}$$

$\mathscr{K}$: Number of all cells

$\mathscr{K}_{CT}$: Number of all cells of cell type CT

$\mathscr{K}nn$: Number of all cells in nearest neighbor of the anchor cell

$\mathscr{K}nn_{CT}$: Number of all cell type CT in nearest neighbor of the anchor cell

$\mathscr{K}nn^{S}$: Number of all selected cells in nearest neighbor of the anchor cell

$\mathscr{K}^{S}$: Number of all selected cells

$\mathscr{K}nn^{S}_{CT}$: Number of all selected cell type CT in nearest neighbor of the anchor cell

$\mathscr{K}^{S}_{CT}$: Number of all selected cell type CT

Distance calculations—Spatial position of each cell (x, y) in the image was calculated by averaging (x_{min}, y_{min}) and (x_{max}, y_{max}) of a given cell according to the single-cell output table derived from HALO. Then, Euclidean distance between MAIT cells and each surrounding cell (as annotated by unsupervised clustering) was computed per patient.

Integration of CODEX and scRNA-seq—For the integration of CODEX and scRNA-seq data, only immune cell clusters were considered. Granulocyte clusters found in CODEX were not included in the analysis, as these cells could not be recovered in our scRNA-seq experiment. The data were integrated with a two-step approach. First, the considered immune-related antigens of the CODEX measurement were mapped to their corresponding genes. This resulted in a shared feature space for both data sets. Second, the mean expression of all clusters was calculated, and the pairwise Pearson correlation between the expression profiles of both sets (CODEX vs. scRNA-seq clusters) was computed.

MAIT + TAM co-culture studies—For co-culture of hepatic MAIT cells with $CD163^{+}$ macrophages, liver tissue was collected from patients undergoing liver resection or liver transplantation, MNCs were isolated as described above. MAIT cells were purified using PE-coupled MR1/5-OP-RU-loaded tetramers and magnetically labeled using anti-PE microbeads (Miltenyi Biotec, Cat.No. 130-048-801) and sorted using an AutoMACS Pro (Miltenyi Bitoech) following the manufacturer's instructions. MAIT-depleted samples were then labeled using a CD163 MicroBead Kit (Miltenyi Biotec, Cat.No. 130-124-420) and $CD163^{+}$ and $CD163^{-}$ cells were separated using the AutoMACS Pro following the manufacturer's instructions. Purified MAITs were then co-cultured with either $CD163^{+}$macrophages or $CD163^{-}$ cells in X-VIVO15 culture media (Lonza, Cat.No. BE02–053Q) supplemented with 2% human serum for 48 hours. For some conditions, clinical grade monoclonal antibody against PD-L1 (Atezolizumab, TECENTRIQ®, Genentech) was added at 20 ug/mL. For some conditions, $CD163^{+}$macrophages were placed on the upper layer of a HTS Transwell® 96-well permeable system (Corning, Cat.No 3380) with 1μm pore size. For intracellular cytokine staining at the end of the incubation period, cells were stimulated for 4h at 37 °C with a commercially available leukocyte activation cocktail (BD Biosciences, catalogue no.550583) containing PMA and ionomycin as well as brefeldin A at

2μL/mL media. Measurement of cytokine production was performed using flow cytometry as described below.

Tumor models—Intrahepatic tumor cell injections were performed as described in detail elsewhere[57]. In brief, cell suspensions of indicated syngeneic tumor cell lines were prepared and resuspended in a 1:1 mix of PBS and Matrigel (Corning, Cat. No. 354230). Intrahepatic tumors were established by injecting 20 μL total volume containing 2–2.5 × 10^5 tumor cells into the left lateral liver lobe. Mice were randomized prior to treatment initiation and tumor size readouts were performed by a blinded examiner.

Targeted knockout of Cd274 in tumor cells using CRISPR/Cas9-mediated gene editing—RIL-175, Hep55.1c, B16-F10 and MC38 tumor cell lines were used for targeted knockout of *Cd274*. Six candidate sgRNAs targeting early protein coding exons of Cd274 (ENSMUST00000016640.7) were designed using sgRNA Scorer 2.0[58]. *In vitro* transcribed candidate guide RNAs were complexed with recombinant Cas9 protein and transfected into P19 cells using Lipofectamine 2000 and editing was assessed using deep amplicon sequencing using methodology previously described[59 58]. Oligonucleotides encoding for the top candidate, 1768 (GGCTCCAAAGGACTTGTACG), were then annealed and ligated into the LentiCRISPRv2-mCherry vector using the T4 rapid ligase (Enzymatics). LentiCRISPRv2-mCherry was a gift from Agata Smogorzewska (Addgene plasmid # 99154 ; http://n2t.net/addgene:99154; RRID:Addgene_99154). The cloned guide RNA plasmid targeting *Cd274* (pGMC00027) has been deposited into Addgene (#199279). The non-targeting control plasmid was generated previously (pGMC00014, Addgene-172526)[12].

Analysis of Cd274 knockout tumor cell clones: Lentiviral vectors encoding for the CRISPR/Cas9 construct, the sgRNA (targeting Cd274 gene locus) and mCherry were transfected into tumor cells using Lipofectamine3000 (Invitrogen) according to the manufacturer's instructions. 72 hours post transfection, transfected cells were harvested, and single cells were sorted into single wells of a 96-well. Monoclonal $Cd274^{-/-}$ cell lines for all parental tumor cell lines were generated and loss of PD-L1 protein surface expression was confirmed by flow cytometry after stimulation with 20 ng/mL IFNγ overnight.

Isolation of murine hepatic and tumor-infiltrating mononuclear cells (MNCs)—Isolation of liver and tumor-infiltrating mononuclear cells followed previously reported protocols[60]. Briefly, tumor-bearing livers were removed and solid tumors growing in the liver were excised. Tumors and livers were processed separately to study differences in hepatic and tumor-infiltrating mononuclear cells. Livers were homogenized and filtered through 70μm nylon mesh. Density-gradient centrifugation using 90% Percoll (Cytiva, catalogue no. 17089109) allows for the separation of MNCs from parenchymal cells. Tumors were homogenized and then further dissociated using a gentleMACS Octo Dissociator (Miltenyi, RRID:SCR_020272). Samples were filtered through 70 μm nylon mesh and subsequently through 40 μm cell strainers prior to density-gradient centrifugation with Lympholyte Cell Separation Media (Cedarlane Laboratories, Cat. No. CL5035). For both liver and tumor samples, red blood lysis was achieved using ACK-lysis buffer (Quality Biologicals, catalogue no. 118–156–101).

To increase the yield for myeloid cells prior to scRNA-seq, we used an *in vivo* enzymatic digestion method to retrieve immune cells from murine livers[35]. Briefly, mice were euthanized, and the portal vein and inferior vena cava (IVC) were canulated with a 22G peripheral IV Catheter (Jelco). The liver was perfused anterogradely with 1x HBSS (ThermoFisher, Cat No 14185052) prior to enzymatic digestion with Collagenase IV (Sigma-Aldrich, Cat.No. C5138) at 0.2 mg/mL and DNase I (Sigma-Aldrich, Cat.No. D5025) at 5U/mL in serum-free RPMI 1640 (ThermoFisher, Cat.No. 11875093) at a flow rate of 5ml/min. Then, the liver was removed and mechanically dissociated using a razor blade, followed by filtering through a 100μm cell strainer. Hepatocytes were pelleted by centrifugation at 50 g for three minutes, which was repeated for the remaining supernatant. After a final centrifugation, red blood lysis was achieved using ACK-lysis buffer (Quality Biologicals, catalogue no. 118–156–101).

Flow cytometry—Murine and human MR1-tetramers loaded with MAIT ligand 5-OP-RU were kindly provided by the NIH tetramer core facility (Emory University). The material was produced by the NIH Tetramer Core Facility as permitted to be distributed by the University of Melbourne. For human samples, Live/Dead staining using Fixable Viability dye ZOMBIE-UV followed by Fc-blocking (BD Biosciences Cat# 564220, RRID:AB_2728082) was performed. The following commercially available anti-human antibodies were used: anti-CD45-Alexa Fluor 700 (Biolegend Cat# 304023, RRID:AB_493760), anti-CD14-V500 (BD Biosciences Cat# 561391, RRID: AB_10611856), anti-CD15-V500 (BD Biosciences Cat# 561585, RRID:AB_10896278), anti-CD19-V500 (BD Biosciences Cat# 561125, RRID:AB_10563208), anti-CD3-PerCP/Cy5.5 (BioLegend Cat# 300430, RRID:AB_893299), anti-CD14-BB515 (BD Biosciences Cat# 564419, RRID: AB_2744419), anti-CD8a-BV605 (BioLegend Cat # 301040, RRID:AB_2563185), anti-TCR Va7.2-PE (BioLegend Cat# 351706, RRID:AB_10899577), anti-CD161-PE/Cy7 (BioLegend Cat# 339918, RRID:AB_11126745), anti-CD56-APC/Fire 750 (BioLegend Cat# 392408, RRID:AB_2728404), anti-CD69-PE-CD594 (BD Biosciences Cat# 562645, RRID:AB_2737699), anti-CD25-APC (BioLegend Cat# 302610, RRID:AB_314280), anti-CD38-BV650 (BioLegend Cat# 356620, RRID:AB_2566233), anti-CD279-BV421 (BioLegend Cat# 329920, RRID:AB_10960742), anti-CD274-BV650 (BD Biosciences Cat# 563740, RRID:AB_2738398), anti-HLA-DR-BV785 (BioLegend Cat# 307641, RRI:AB_2561360), anti-CD206-PE (BioLegend Cat# 321106, RRID:AB_571911), anti-CD14-APC (BD Biosciences Cat# 561383, RRID: AB_1061200), anti-CD11b-PerCP/Cy5.5 (BioLegend Cat# 301327, RRID:AB_10900072), anti-CD163-FITC (BD Biosciences Cat# 563697 RRID:AB_2738379), anti-CD3-BV421 (BD Biosciences Cat# 562426, RRID:AB_11152082), anti-CD19-BV421 (BioLegend Cat# 302234, RRID:AB_11142678), anti-CD68-PE/Cy7 (BD Biosciences Cat# 565595, RRID:AB_2739298), anti-CD11c-BV510 (BD Biosciences Cat# 563026, RRID:AB_2737960).

Murine samples were stained as follows: Live/Dead staining using Fixable Viability dye ZOMBIE-UV (Biolegend, Cat. No. 423108) for 20 min at 4 °C was followed by Fc-blocking (Biolegend, catalogue no. 101302) for 15 minutes at 4°C. Antibody surface staining as well as tetramer staining was performed by incubating 1–2 × 10^6 cells at 37 °C (for murine MR1

tetramers) or 4 °C (for human MR1 tetramers) for 30 min in staining buffer (BD Bioscience, catalogue no. 554656). The following commercially available anti-mouse antibodies were used: anti-CD62L-PerCP/Cy5.5 (BioLegend Cat# 104432, RRID:AB_2285839), anti-CD44-PE/Cy7 (BioLegend Cat# 103030, RRID:AB_830787), anti-CD69-BV650 (BioLegend Cat# 104541, RRID:AB_2616934), anti-TCRβ-APC/Fire 750 (BioLegend Cat# 109246, RRID:AB_2629697), anti-NK1.1-PE (BioLegend Cat# 108708, RRID:AB_313395), anti-F4/80-Alexa Fluor 700 (BioLegend Cat# 123130, RRID:AB_2293450), anti-B220-Alexa Fluor 700 (BioLegend Cat# 103232, RRID:AB_493717), anti-CD11b-Alexa Fluor 700 (BioLegend Cat# 101222, RRID:AB_493705), anti-CD3-Alexa Fluor 594 (BioLegend Cat# 100240, RRID:AB_2563427), anti-CD4-BV605 (BioLegend Cat# 100451, RRID:AB_2564591), anti-CD4-AF700 (BD Biosciences Cat# 557956, RRID: AB_396956), anti-CD8-BV786 (BD Biosciences Cat# 563332, RRID:AB_2721167), anti-CD11b-Pacific Blue (BioLegend Cat# 101224, RRID:AB_755986), anti-Ly-6G-Alexa Fluor 700 (BioLegend Cat# 127622, RRID:AB_10643269), anti-Ly-6C-APC/Cy7 (BioLegend Cat# 128026, RRID:AB_10640120), ki67 (BioLegend, Cat.# 652411, RRID: AB_2562663), RoRyt (Invitrogen, Cat# 12–6981–82, RRID: AB_10807092), T-bet (BioLegend Cat. No. 644824, RRID: AB_2561761) and anti-FOXP3-APC (Thermo Fisher Scientific Cat# 17–5773–82, RRID:AB_469457). Murine MAIT cells were defined by flow cytometry as $B220^{-}F4/80^{-}CD11b^{-}CD3^{+}TCRb^{int}$MR1/5-OP-RU tetramer^{+}

For intracellular cytokine staining, cells were stimulated for 4h at 37 °C with a commercially available leukocyte activation cocktail (BD Biosciences, catalogue no.550583) containing PMA and ionomycin as well as brefeldin A at a concentration of 2 μL/mL. After surface staining, cells were fixed and permeabilized using a Fixation/Permeabilization Solution Kit (eBioscience, catalogue no. 88–8824–00). Cells were incubated in permeabilization buffer (as part of the abovementioned kit) containing the following fluorochrome-labeled antibodies for half an hour at 4 °C: anti-IFN-γ-APC (BioLegend Cat# 505810, RRID:AB_315404), anti-Perforin-APC (BioLegend Cat# 154304, RRID:AB_2721463), anti-Granzyme B-FITC (BioLegend Cat# 515403, RRID:AB_2114575), anti-IL17A-FITC (BioLegend Cat# 506908, RRID:AB_536010).

Data for all samples were collected on a CytoFLEX LX flow cytometer (Beckman Coulter CytoFLEX Flow Cytometer, RRID:SCR_019627) and analyzed using FlowJo software (FlowJo, RRID:SCR_008520).

Quantification and Statistical Analysis—Sample sizes for animal studies were guided by previous studies with similar or identical tumor models. The majority of experiments were repeated at least twice to obtain robust data for indicated statistical analyses. For all readouts, examiners were blinded. Statistical analysis was performed using GraphPad Prism 9 (GraphPad Prism, RRID:SCR_002798). Experimental groups were compared by paired or unpaired two-tailed Student's t test with a 95% confidence interval or One-Way ANOVA (Tukey's multiple comparison test). Non-parametric Mann–Whitney U or Kruskal–Wallis test (Dunn's multiple comparison test) were applied if data sets failed the D'Agostino & Pearson normality test (or Shapiro–Wilk normality test for small n). n.s.: not significant for $p > .05$; *$p < .05$; **$p < .01$; ***$p < .001$; ****$p < .0001$).

Supplementary Material

Refer to Web version on PubMed Central for supplementary material.

ACKNOWLEDGEMENTS

The MR1 tetramer technology was developed jointly by Dr. James McCluskey, Dr. Jamie Rossjohn, and Dr. David Fairlie.

We are grateful to Sophie Wang, Dr. Daniel Barber, Dr. Shunsuke Sakai (both NIAID) and Dr. Stephen Hewitt, Dr. Natalie Porat-Shliom, Dr. Jay Berzofsky and Dr. Camille A. Spinner (all NCI).

We thank Dr. Amaia Lujambio (Mount Sinaii), Dr. Clifton Barry III and Dr. Sangmi Oh (NIAID) for providing critical reagents.

The results published here are in part based on data generated by the TCGA Research Network: http://cancergenome.nih.gov/.

Support from CCR Single Cell Analysis Facility was funded by FNLCR Contract 75N91019D00024. Sequencing was performed in conjunction with the CCR Genomics Core. This work utilized the computational resources of the NIH HPC Biowulf cluster. (http://hpc.nih.gov). We thank Ian Taukulis and Dr. Michael Kelly for assistance with the single-cell RNA-seq datasets.

Analysis and management of images and associated metadata was supported in part by the NCI HALO Image Analysis Resource. We thank Dr. Janelle Cortner, Mr. Aras Eftekhari, Duncan Donohue, Dr. Kathleen Calzone and Dr. Sunita Menon for assistance with depositing the primary data.

Grant support:

B.R. was supported by the International Liver Cancer Association (ILCA) Fellowship Award 2021, M.B. was funded by the Deutsche Forschungsgemeinschaft (DFG) under Germany's Excellence Strategy – EXC number 2064/1 and International Max Planck Research School for Intelligent Systems (IMPRS-IS). S.B. was funded by the DFG under Germany's Excellence Strategy – EXC number 2180. N.K was supported by the Intramural Research Program of the NIH, NCI (ZIC BC 011434). S.W. was funded by the DFG (WA-4610/1-1), A.K. acknowledges funding support from the National Institute of Allergy and Infectious Diseases (R01AI132389; R21AI130800). R.C is supported by the NIH, under Contract No. HHSN261201500003I. X.W.W. was supported by the Intramural Research program (IRP) of the NIH, NCI (ZIA BC 010313). T.F.G. was supported by the IRP of the NIH, NCI (ZIA BC 011345).

INCLUSION AND DIVERSITY

We support inclusive, diverse, and equitable conduct of research. We worked to ensure ethnic or other types of diversity in the recruitment of human subjects. We worked to ensure sex balance in the selection of non-human subjects. One or more of the authors of this paper self-identifies as an underrepresented ethnic minority in their field of research or within their geographical location. One or more of the authors of this paper self-identifies as a gender minority in their field of research. One or more of the authors of this paper self-identifies as a member of the LGBTQIA+ community. One or more of the authors of this paper received support from a program designed to increase minority representation in their field of research. We avoided "helicopter science" practices by including the participating local contributors from the region where we conducted the research as authors on the paper.

REFERENCES

1. Llovet JM, Zucman-Rossi J, Pikarsky E, Sangro B, Schwartz M, Sherman M, and Gores G (2016). Hepatocellular carcinoma. Nat Rev Dis Primers 2, 16018. 10.1038/nrdp.2016.18. [PubMed: 27158749]

2. Llovet JM, Castet F, Heikenwalder M, Maini MK, Mazzaferro V, Pinato DJ, Pikarsky E, Zhu AX, and Finn RS (2022). Immunotherapies for hepatocellular carcinoma. Nature reviews. Clinical oncology 19, 151–172. 10.1038/s41571-021-00573-2.

3. Greten TF, Abou-Alfa GK, Cheng AL, Duffy AG, El-Khoueiry AB, Finn RS, Galle PR, Goyal L, He AR, Kaseb AO, et al. (2021). Society for Immunotherapy of Cancer (SITC) clinical practice guideline on immunotherapy for the treatment of hepatocellular carcinoma. J Immunother Cancer 9. 10.1136/jitc-2021-002794.

4. Sangro B, Sarobe P, Hervas-Stubbs S, and Melero I (2021). Advances in immunotherapy for hepatocellular carcinoma. Nat Rev Gastroenterol Hepatol 18, 525–543. 10.1038/s41575-021-00438-0. [PubMed: 33850328]

5. Treiner E, Duban L, Bahram S, Radosavljevic M, Wanner V, Tilloy F, Affaticati P, Gilfillan S, and Lantz O (2003). Selection of evolutionarily conserved mucosal-associated invariant T cells by MR1. Nature 422, 164–169. 10.1038/nature01433. [PubMed: 12634786]

6. Dusseaux M, Martin E, Serriari N, Peguillet I, Premel V, Louis D, Milder M, Le Bourhis L, Soudais C, Treiner E, and Lantz O (2011). Human MAIT cells are xenobiotic-resistant, tissue-targeted, CD161hi IL-17-secreting T cells. Blood 117, 1250–1259. 10.1182/blood-2010-08-303339. [PubMed: 21084709]

7. Rahimpour A, Koay HF, Enders A, Clanchy R, Eckle SB, Meehan B, Chen Z, Whittle B, Liu L, Fairlie DP, et al. (2015). Identification of phenotypically and functionally heterogeneous mouse mucosal-associated invariant T cells using MR1 tetramers. The Journal of experimental medicine 212, 1095–1108. 10.1084/jem.20142110. [PubMed: 26101265]

8. Duan M, Goswami S, Shi JY, Wu LJ, Wang XY, Ma JQ, Zhang Z, Shi Y, Ma LJ, Zhang S, et al. (2019). Activated and Exhausted MAIT Cells Foster Disease Progression and Indicate Poor Outcome in Hepatocellular Carcinoma. Clinical cancer research : an official journal of the American Association for Cancer Research 25, 3304–3316. 10.1158/1078-0432.CCR-18-3040. [PubMed: 30723143]

9. Zimmer CL, Filipovic I, Cornillet M, O'Rourke CJ, Berglin L, Jansson H, Sun D, Strauss O, Hertwig L, Johansson H, et al. (2022). Mucosal-associated invariant T-cell tumor infiltration predicts long-term survival in cholangiocarcinoma. Hepatology (Baltimore, Md.) 75, 1154–1168. 10.1002/hep.32222.

10. Yan J, Allen S, McDonald E, Das I, Mak JYW, Liu L, Fairlie DP, Meehan BS, Chen Z, Corbett AJ, et al. (2020). MAIT Cells Promote Tumor Initiation, Growth, and Metastases via Tumor MR1. Cancer Discov 10, 124–141. 10.1158/2159-8290.CD-19-0569. [PubMed: 31826876]

11. Petley EV, Koay HF, Henderson MA, Sek K, Todd KL, Keam SP, Lai J, House IG, Li J, Zethoven M, et al. (2021). MAIT cells regulate NK cell-mediated tumor immunity. Nat Commun 12, 4746. 10.1038/s41467-021-25009-4. [PubMed: 34362900]

12. Ruf B, Catania VV, Wabitsch S, Ma C, Diggs LP, Zhang Q, Heinrich B, Subramanyam V, Cui LL, Pouzolles M, et al. (2021). Activating Mucosal-Associated Invariant T Cells Induces a Broad Antitumor Response. Cancer Immunol Res 9, 1024–1034. 10.1158/2326-6066.CIR-20-0925. [PubMed: 34193462]

13. Zhang Q, He Y, Luo N, Patel SJ, Han Y, Gao R, Modak M, Carotta S, Haslinger C, Kind D, et al. (2019). Landscape and Dynamics of Single Immune Cells in Hepatocellular Carcinoma. Cell 179, 829–845 e820. 10.1016/j.cell.2019.10.003. [PubMed: 31675496]

14. Sun Y, Wu L, Zhong Y, Zhou K, Hou Y, Wang Z, Zhang Z, Xie J, Wang C, Chen D, et al. (2021). Single-cell landscape of the ecosystem in early-relapse hepatocellular carcinoma. Cell 184, 404–421 e416. 10.1016/j.cell.2020.11.041. [PubMed: 33357445]

15. Yao T, Shooshtari P, and Haeryfar SMM (2020). Leveraging Public Single-Cell and Bulk Transcriptomic Datasets to Delineate MAIT Cell Roles and Phenotypic Characteristics in Human Malignancies. Frontiers in immunology 11, 1691. 10.3389/fimmu.2020.01691. [PubMed: 32849590]

16. Zheng C, Zheng L, Yoo JK, Guo H, Zhang Y, Guo X, Kang B, Hu R, Huang JY, Zhang Q, et al. (2017). Landscape of Infiltrating T Cells in Liver Cancer Revealed by Single-Cell Sequencing. Cell 169, 1342–1356 e1316. 10.1016/j.cell.2017.05.035. [PubMed: 28622514]

17. Li S, Simoni Y, Becht E, Loh CY, Li N, Lachance D, Koo SL, Lim TP, Tan EKW, Mathew R, et al. (2020). Human Tumor-Infiltrating MAIT Cells Display Hallmarks of Bacterial Antigen

Recognition in Colorectal Cancer. Cell Rep Med 1, 100039. 10.1016/j.xcrm.2020.100039. [PubMed: 33205061]

18. Salou M, Legoux F, Gilet J, Darbois A, du Halgouet A, Alonso R, Richer W, Goubet AG, Daviaud C, Menger L, et al. (2019). A common transcriptomic program acquired in the thymus defines tissue residency of MAIT and NKT subsets. The Journal of experimental medicine 216, 133–151. 10.1084/jem.20181483. [PubMed: 30518599]
19. Huang W, Ye D, He W, He X, Shi X, and Gao Y (2021). Activated but impaired IFN-gamma production of mucosal-associated invariant T cells in patients with hepatocellular carcinoma. J Immunother Cancer 9. 10.1136/jitc-2021-003685.
20. Garner LC, Klenerman P, and Provine NM (2018). Insights Into Mucosal-Associated Invariant T Cell Biology From Studies of Invariant Natural Killer T Cells. Frontiers in immunology 9, 1478. 10.3389/fimmu.2018.01478. [PubMed: 30013556]
21. Philip M, and Schietinger A (2022). CD8(+) T cell differentiation and dysfunction in cancer. Nature reviews. Immunology 22, 209–223. 10.1038/s41577-021-00574-3.
22. Molina-Sanchez P, Ruiz de Galarreta M, Yao MA, Lindblad KE, Bresnahan E, Bitterman E, Martin TC, Rubenstein T, Nie K, Golas J, et al. (2020). Cooperation Between Distinct Cancer Driver Genes Underlies Intertumor Heterogeneity in Hepatocellular Carcinoma. Gastroenterology 159, 2203–2220 e2214. 10.1053/j.gastro.2020.08.015. [PubMed: 32814112]
23. Goltsev Y, Samusik N, Kennedy-Darling J, Bhate S, Hale M, Vazquez G, Black S, and Nolan GP (2018). Deep Profiling of Mouse Splenic Architecture with CODEX Multiplexed Imaging. Cell 174, 968–981 e915. 10.1016/j.cell.2018.07.010. [PubMed: 30078711]
24. Black S, Phillips D, Hickey JW, Kennedy-Darling J, Venkataraaman VG, Samusik N, Goltsev Y, Schurch CM, and Nolan GP (2021). CODEX multiplexed tissue imaging with DNA-conjugated antibodies. Nature protocols 16, 3802–3835. 10.1038/s41596-021-00556-8. [PubMed: 34215862]
25. Bald T, Krummel MF, Smyth MJ, and Barry KC (2020). The NK cell-cancer cycle: advances and new challenges in NK cell-based immunotherapies. Nat Immunol 21, 835–847. 10.1038/s41590-020-0728-z. [PubMed: 32690952]
26. Schurch CM, Bhate SS, Barlow GL, Phillips DJ, Noti L, Zlobec I, Chu P, Black S, Demeter J, McIlwain DR, et al. (2020). Coordinated Cellular Neighborhoods Orchestrate Antitumoral Immunity at the Colorectal Cancer Invasive Front. Cell 182, 1341–1359 e1319. 10.1016/j.cell.2020.07.005. [PubMed: 32763154]
27. Liudahl SM, Betts CB, Sivagnanam S, Morales-Oyarvide V, da Silva A, Yuan C, Hwang S, Grossblatt-Wait A, Leis KR, Larson W, et al. (2021). Leukocyte Heterogeneity in Pancreatic Ductal Adenocarcinoma: Phenotypic and Spatial Features Associated with Clinical Outcome. Cancer Discov 11, 2014–2031. 10.1158/2159-8290.CD-20-0841. [PubMed: 33727309]
28. Thommen DS, and Schumacher TN (2018). T Cell Dysfunction in Cancer. Cancer Cell 33, 547–562. 10.1016/j.ccell.2018.03.012. [PubMed: 29634943]
29. Babaei S, Christ J, Makky A, Zidane M, Wistuba-Hamprecht K, Schürch CM, and Claassen M (2023). S^3-CIMA: Supervised spatial single-cell image analysis for the identification of disease-associated cell type compositions in tissue. bioRxiv, 2023.2003.2017.533167. 10.1101/2023.03.17.533167.
30. Amores J (2013). Multiple instance classification: Review, taxonomy and comparative study. Artificial Intelligence 201, 81–105. 10.1016/j.artint.2013.06.003.
31. LeCun Y, Bengio Y, and Hinton G (2015). Deep learning. Nature 521, 436–444. 10.1038/nature14539. [PubMed: 26017442]
32. Yeung OW, Lo CM, Ling CC, Qi X, Geng W, Li CX, Ng KT, Forbes SJ, Guan XY, Poon RT, et al. (2015). Alternatively activated (M2) macrophages promote tumour growth and invasiveness in hepatocellular carcinoma. Journal of hepatology 62, 607–616. 10.1016/j.jhep.2014.10.029. [PubMed: 25450711]
33. Wu K, Kryczek I, Chen L, Zou W, and Welling TH (2009). Kupffer cell suppression of CD8+ T cells in human hepatocellular carcinoma is mediated by B7-H1/programmed death-1 interactions. Cancer research 69, 8067–8075. 10.1158/0008-5472.CAN-09-0901. [PubMed: 19826049]
34. Ma L, Wang L, Khatib SA, Chang CW, Heinrich S, Dominguez DA, Forgues M, Candia J, Hernandez MO, Kelly M, et al. (2021). Single-cell atlas of tumor cell evolution in response to

therapy in hepatocellular carcinoma and intrahepatic cholangiocarcinoma. Journal of hepatology 75, 1397–1408. 10.1016/j.jhep.2021.06.028. [PubMed: 34216724]

35. Guilliams M, Bonnardel J, Haest B, Vanderborght B, Wagner C, Remmerie A, Bujko A, Martens L, Thone T, Browaeys R, et al. (2022). Spatial proteogenomics reveals distinct and evolutionarily conserved hepatic macrophage niches. Cell 185, 379–396 e338. 10.1016/j.cell.2021.12.018. [PubMed: 35021063]
36. Schreiber HA, Loschko J, Karssemeijer RA, Escolano A, Meredith MM, Mucida D, Guermonprez P, and Nussenzweig MC (2013). Intestinal monocytes and macrophages are required for T cell polarization in response to Citrobacter rodentium. The Journal of experimental medicine 210, 2025–2039. 10.1084/jem.20130903. [PubMed: 24043764]
37. Sundstrom P, Ahlmanner F, Akeus P, Sundquist M, Alsen S, Yrlid U, Borjesson L, Sjoling A, Gustavsson B, Wong SB, and Quiding-Jarbrink M (2015). Human Mucosa-Associated Invariant T Cells Accumulate in Colon Adenocarcinomas but Produce Reduced Amounts of IFN-gamma. Journal of immunology (Baltimore, Md. : 1950) 195, 3472–3481. 10.4049/jimmunol.1500258. [PubMed: 26297765]
38. Risom T, Glass DR, Averbukh I, Liu CC, Baranski A, Kagel A, McCaffrey EF, Greenwald NF, Rivero-Gutierrez B, Strand SH, et al. (2022). Transition to invasive breast cancer is associated with progressive changes in the structure and composition of tumor stroma. Cell 185, 299–310 e218. 10.1016/j.cell.2021.12.023. [PubMed: 35063072]
39. Hickey JW, Tan Y, Nolan GP, and Goltsev Y (2021). Strategies for Accurate Cell Type Identification in CODEX Multiplexed Imaging Data. Frontiers in immunology 12, 727626. 10.3389/fimmu.2021.727626. [PubMed: 34484237]
40. Toubal A, Kiaf B, Beaudoin L, Cagninacci L, Rhimi M, Fruchet B, da Silva J, Corbett AJ, Simoni Y, Lantz O, et al. (2020). Mucosal-associated invariant T cells promote inflammation and intestinal dysbiosis leading to metabolic dysfunction during obesity. Nat Commun 11, 3755. 10.1038/s41467-020-17307-0. [PubMed: 32709874]
41. Li Y, Huang B, Jiang X, Chen W, Zhang J, Wei Y, Chen Y, Lian M, Bian Z, Miao Q, et al. (2018). Mucosal-Associated Invariant T Cells Improve Nonalcoholic Fatty Liver Disease Through Regulating Macrophage Polarization. Frontiers in immunology 9, 1994. 10.3389/fimmu.2018.01994. [PubMed: 30233587]
42. Flament H, Rouland M, Beaudoin L, Toubal A, Bertrand L, Lebourgeois S, Rousseau C, Soulard P, Gouda Z, Cagninacci L, et al. (2021). Outcome of SARS-CoV-2 infection is linked to MAIT cell activation and cytotoxicity. Nat Immunol 22, 322–335. 10.1038/s41590-021-00870-z. [PubMed: 33531712]
43. Meierovics AI, and Cowley SC (2016). MAIT cells promote inflammatory monocyte differentiation into dendritic cells during pulmonary intracellular infection. The Journal of experimental medicine 213, 2793–2809. 10.1084/jem.20160637. [PubMed: 27799620]
44. Provine NM, Amini A, Garner LC, Spencer AJ, Dold C, Hutchings C, Silva Reyes L, FitzPatrick MEB, Chinnakannan S, Oguti B, et al. (2021). MAIT cell activation augments adenovirus vector vaccine immunogenicity. Science (New York, N.Y.) 371, 521–526. 10.1126/science.aax8819. [PubMed: 33510029]
45. Vorwald VM, Davis DM, Van Gulick RJ, Torphy RJ, Borgers JS, Klarquist J, Couts KL, Amato CM, Cogswell DT, Fujita M, et al. (2022). Circulating CD8(+) mucosal-associated invariant T cells correlate with improved treatment responses and overall survival in anti-PD-1-treated melanoma patients. Clin Transl Immunology 11, e1367. 10.1002/cti2.1367. [PubMed: 35028137]
46. De Biasi S, Gibellini L, Lo Tartaro D, Puccio S, Rabacchi C, Mazza EMC, Brummelman J, Williams B, Kaihara K, Forcato M, et al. (2021). Circulating mucosal-associated invariant T cells identify patients responding to anti-PD-1 therapy. Nat Commun 12, 1669. 10.1038/s41467-021-21928-4. [PubMed: 33723257]
47. Heinrich B, Gertz EM, Schaffer AA, Craig A, Ruf B, Subramanyam V, McVey JC, Diggs LP, Heinrich S, Rosato U, et al. (2022). The tumour microenvironment shapes innate lymphoid cells in patients with hepatocellular carcinoma. Gut 71, 1161–1175. 10.1136/gutjnl-2021-325288. [PubMed: 34340996]

48. Sakai S, Kauffman KD, Oh S, Nelson CE, Barry CE 3rd, and Barber DL (2021). MAIT cell-directed therapy of Mycobacterium tuberculosis infection. Mucosal Immunol 14, 199–208. 10.1038/s41385-020-0332-4. [PubMed: 32811991]

49. Kapanadze T, Gamrekelashvili J, Ma C, Chan C, Zhao F, Hewitt S, Zender L, Kapoor V, Felsher DW, Manns MP, et al. (2013). Regulation of accumulation and function of myeloid derived suppressor cells in different murine models of hepatocellular carcinoma. Journal of hepatology 59, 1007–1013. 10.1016/j.jhep.2013.06.010. [PubMed: 23796475]

50. Korsunsky I, Millard N, Fan J, Slowikowski K, Zhang F, Wei K, Baglaenko Y, Brenner M, Loh PR, and Raychaudhuri S (2019). Fast, sensitive and accurate integration of single-cell data with Harmony. Nat Methods 16, 1289–1296. 10.1038/s41592-019-0619-0. [PubMed: 31740819]

51. Traag VA, Waltman L, and van Eck NJ (2019). From Louvain to Leiden: guaranteeing well-connected communities. Sci Rep 9, 5233. 10.1038/s41598-019-41695-z. [PubMed: 30914743]

52. Blondel VD, Guillaume J-L, Lambiotte R, and Lefebvre E (2008). Fast unfolding of communities in large networks. Journal of Statistical Mechanics: Theory and Experiment 2008, P10008. 10.1088/1742-5468/2008/10/p10008.

53. Roessler S, Jia HL, Budhu A, Forgues M, Ye QH, Lee JS, Thorgeirsson SS, Sun Z, Tang ZY, Qin LX, and Wang XW (2010). A unique metastasis gene signature enables prediction of tumor relapse in early-stage hepatocellular carcinoma patients. Cancer research 70, 10202–10212. 10.1158/0008-5472.CAN-10-2607. [PubMed: 21159642]

54. Chaisaingmongkol J, Budhu A, Dang H, Rabibhadana S, Pupacdi B, Kwon SM, Forgues M, Pomyen Y, Bhudhisawasdi V, Lertprasertsuke N, et al. (2017). Common Molecular Subtypes Among Asian Hepatocellular Carcinoma and Cholangiocarcinoma. Cancer Cell 32, 57–70 e53. 10.1016/j.ccell.2017.05.009. [PubMed: 28648284]

55. Lin J-R, Wang S, Coy S, Chen Y-A, Yapp C, Tyler M, Nariya MK, Heiser CN, Lau KS, Santagata S, and Sorger PK (2022). Multiplexed 3D atlas of state transitions and immune interactions in colorectal cancer. bioRxiv, 2021.2003.2031.437984. 10.1101/2021.03.31.437984.

56. Team, R.D. (2018). RAPIDS: Collection of Libraries for End to End GPU Data Science.

57. Brown ZJ, Heinrich B, and Greten TF (2018). Establishment of Orthotopic Liver Tumors by Surgical Intrahepatic Tumor Injection in Mice with Underlying Non-Alcoholic Fatty Liver Disease. Methods and protocols 1. 10.3390/mps1020021.

58. Chari R, Yeo NC, Chavez A, and Church GM (2017). sgRNA Scorer 2.0: A Species-Independent Model To Predict CRISPR/Cas9 Activity. ACS Synth Biol 6, 902–904. 10.1021/acssynbio.6b00343. [PubMed: 28146356]

59. Gooden AA, Evans CN, Sheets TP, Clapp ME, and Chari R (2021). dbGuide: a database of functionally validated guide RNAs for genome editing in human and mouse cells. Nucleic Acids Res 49, D871–D876. 10.1093/nar/gkaa848. [PubMed: 33051688]

60. Heinrich B, Brown ZJ, Diggs LP, Vormehr M, Ma C, Subramanyam V, Rosato U, Ruf B, Walz JS, McVey JC, et al. (2021). Steatohepatitis Impairs T-cell-Directed Immunotherapies Against Liver Tumors in Mice. Gastroenterology 160, 331–345 e336. 10.1053/j.gastro.2020.09.031. [PubMed: 33010248]

HIGHLIGHTS

- HCC patient sample profiles by flow cytometry, scRNA-seq, imaging, and machine-learning
- MAITs in HCC show impaired tumor infiltration, dysfunction, and loss-of-cytotoxicity
- TAMs impact MAIT cell function through interaction at the tumor-to-liver interface
- aPD-1/aPD-L1 directed therapies target MAITs in HCC.

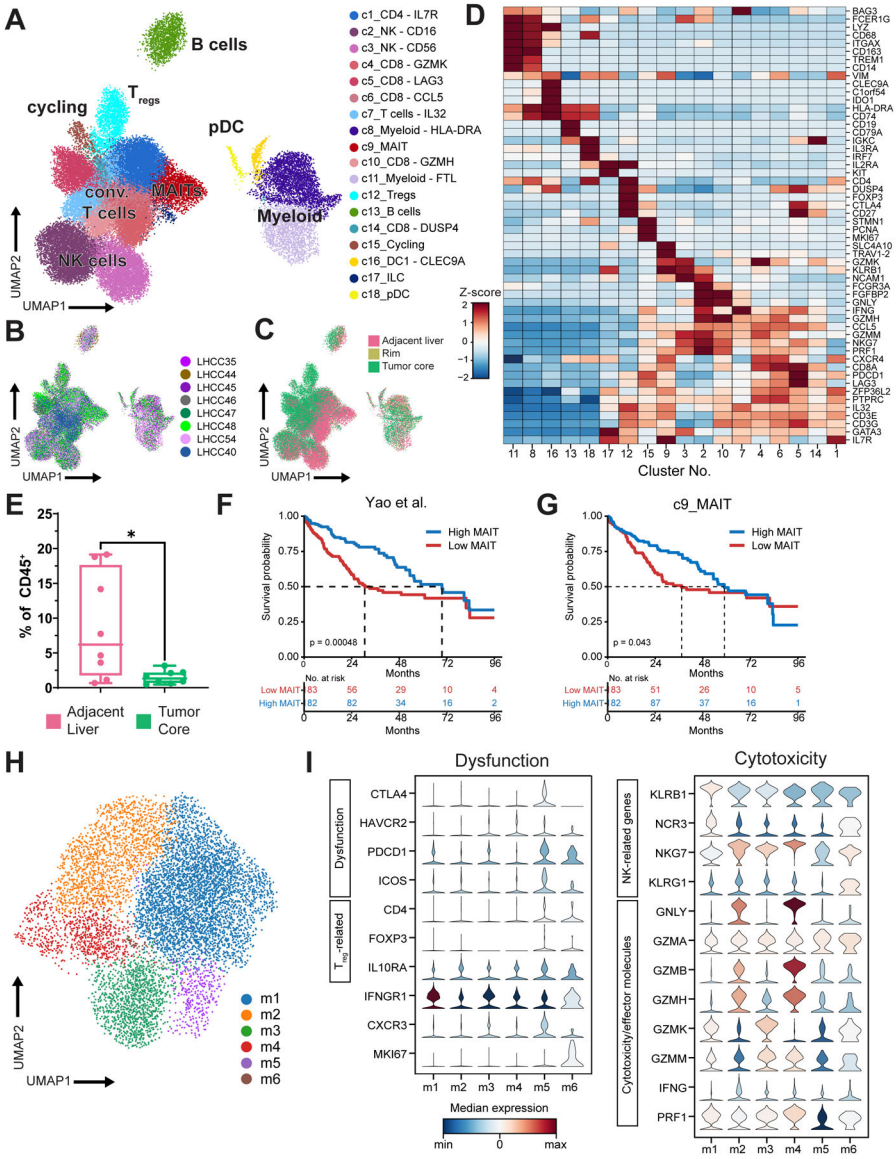

Figure 1. Single-cell RNA sequencing reveals MAIT cell heterogeneity within the HCC bearing liver

(A) Uniform Manifold Approximation and Projection (UMAP) plot, showing clustering for different CD45^{+} immune cell types.

(B) & (C) UMAP plots showing origin of single cells by patients **(B)** and tissue location (**C**).

(D) Heatmap projections showing expression of selected indicated marker genes (corresponding to **A**)

(E) Boxplot displaying frequency of main MAIT cell cluster, c9 amongst T cells.

(F&G) Overall survival (OS) risk probability based on high or low expression of MAIT cell gene signature in TCGA using the MAIT signature by Yao et al. **(F)** or the MAIT signature derived from cluster c9 **(G)**.

(H) UMAP plot showing different MAIT cell subclusters.

(I) Violin plots showing expression of selected markers of dysfunction and cytotoxicity in MAIT cell subclusters (as defined in **H**).

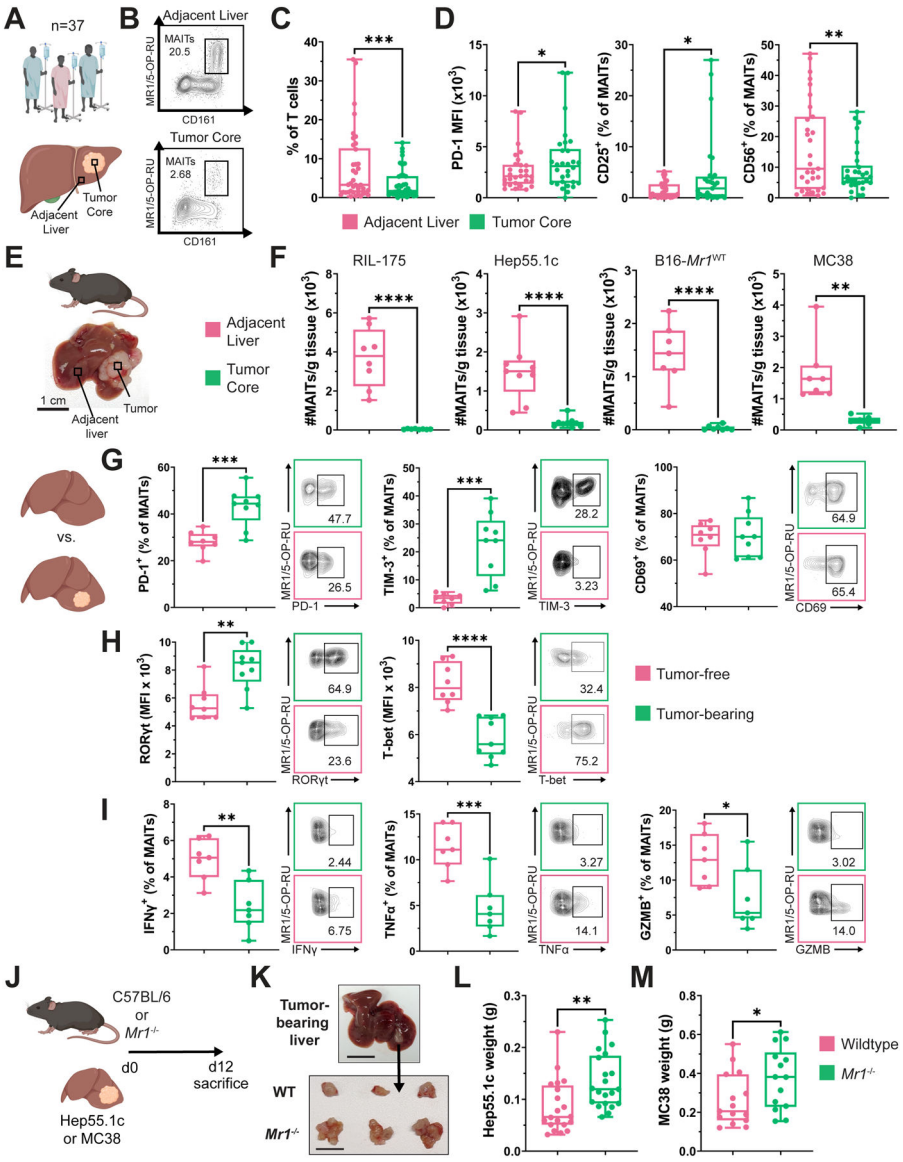

Figure 2: MAIT cells are dysregulated in human and mouse HCC.

(A) Patient cohort & sampling strategy.

(B) Representative flow cytometry plots showing identification of human hepatic MAIT cells (see also Fig.S4A)

(C) Boxplot displaying MAIT cell frequencies as determined by flow cytometry (n=37).

(D) Boxplots showing mean fluorescence intensity (MFI) of PD-1 (left), frequency of $CD25^+$ (middle) and frequency of $CD56^+$ hepatic MAIT cells as determined by flow cytometry (n=37).

(E) Mouse model of syngeneic, orthotopic liver cancer. Photo showing mouse liver with intrahepatic HCC tumor.

(F) Boxplots showing numbers of hepatic and tumor-infiltrating MAIT cells/g tissue. Results for for different tumor cell lines RIL-175, Hep55.1c, MC38 and B16-*Mr1*^{WT} are shown.

(G) Frequency of PD-1^{+} (left), TIM-3^{+} (middle) and CD69^{+} (right) hepatic MAIT. Representative flow cytometry dot plots are shown

(H) Boxplots showing MFI of transcription factors RORγt (left) and T-bet (right) in hepatic MAIT cells at d28. Comparison between tumor-free (n=8) vs tumor-bearing (n=9) mice.

(I) Boxplots showing frequency of cytokines IFNy (left), TNFα (middle) and granzyme B (right) in hepatic MAIT cells. Comparison between tumor-free (n=7) vs tumor-bearing (n=7) mice. Representative flow cytometry dot plots are shown.

(J) Mouse model of syngeneic, orthotopic liver cancer comparing tumor growth in C56BL/6 (Wildtype) and *Mr1*$^{-/-}$ mice.

(K) Top: Photo showing murine liver with a single orthotopic HCC lesion. Bottom: excised intrahepatic tumors comparing WT and *Mr1*$^{-/-}$ mice.

(L) Box plot showing the weight of intrahepatic Hep55.1c tumors at d12 comparing wildtype (n=20) and Mr1$^{-/-}$ mice (n=21).

(M) Box plot showing the weight of intrahepatic MC38 tumors at d12 comparing WT (n=15) and *Mr1*$^{-/-}$ mice (n=14).

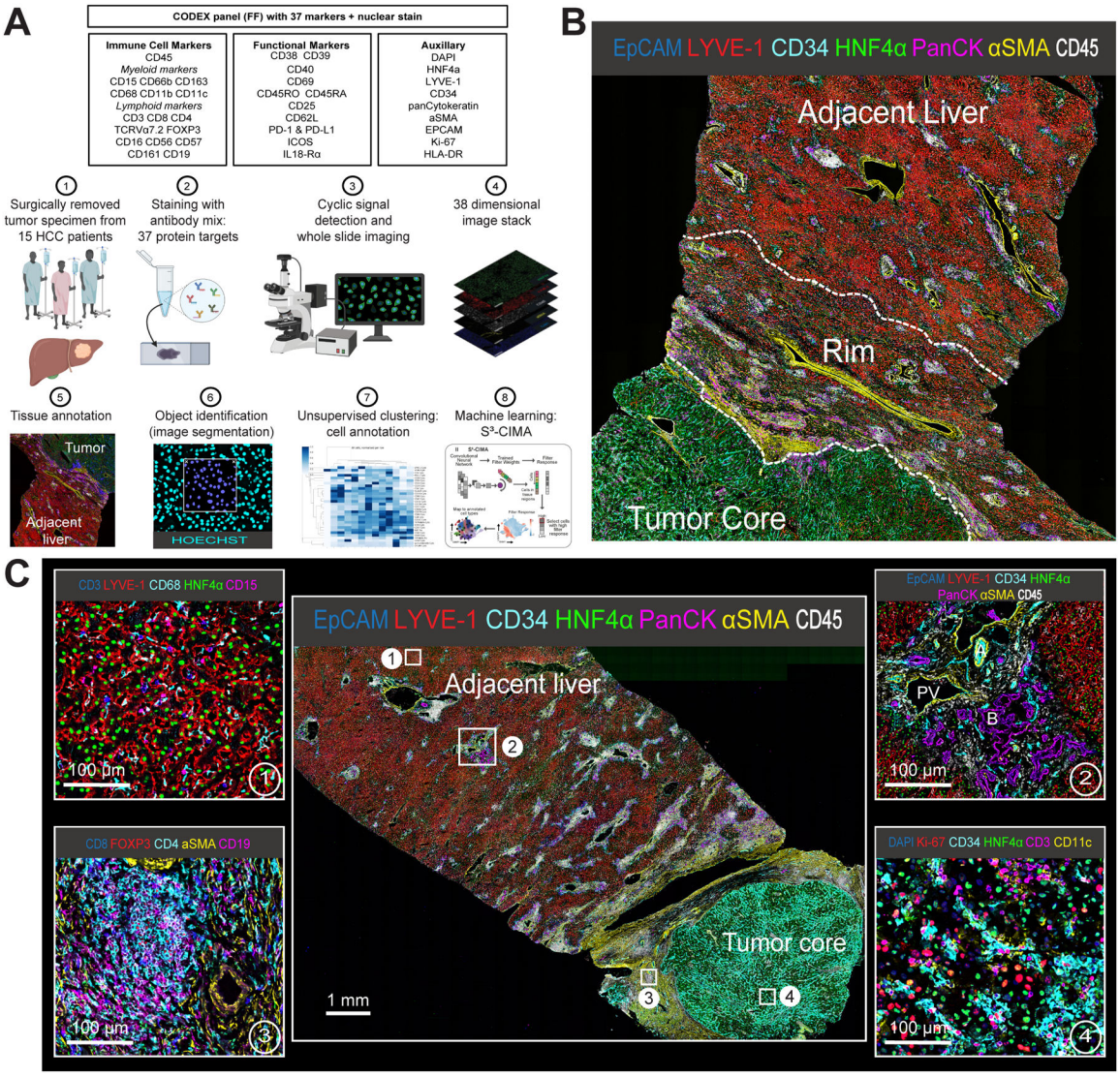

Figure 3: Generation of a spatially resolved immune cell atlas of human liver cancer by CODEX technology

(A) Antibody panel design and CODEX workflow

(B) Seven-color overview of a human HCC sample LHCC35, stained with the 37-plex CODEX panel (see **A**). Representative annotation of gross tissue regions is shown.

(C) Middle: Seven-color overview of a whole tissue section derived from LHCC41. ROI are labeled 1–4 and correspond to higher-magnification multi-color images. ① liver parenchyma in the adjacent liver: T cells ($CD3^+$), granulocytes ($CD15^+$) and macrophages ($CD68^+$) patrol inside the liver sinusoids ($LYVE\text{-}1^+$). ② Periportal region showing branches of the portal vein (PV), arteria hepatic (A) and bile ducts ($EPCAM^+panCK^+$, B). ③ Tertiary lymphoid structure in the rim regions with aggregates of B cells ($CD19^+$), helper T cells ($CD4^+$), regulatory T cells ($FOXP3^+$) and cytotoxic T cells ($CD8^+$) within an aSMA-rich environment. ④ ROI in the tumor core shows proliferating ($Ki\text{-}67^+$) tumor cells ($HNF4a^+$) in an endothelial cell-rich ($CD34^+$) environment. T cells ($CD3^+$) and dendritic cells ($CD11c^+$) are also shown.

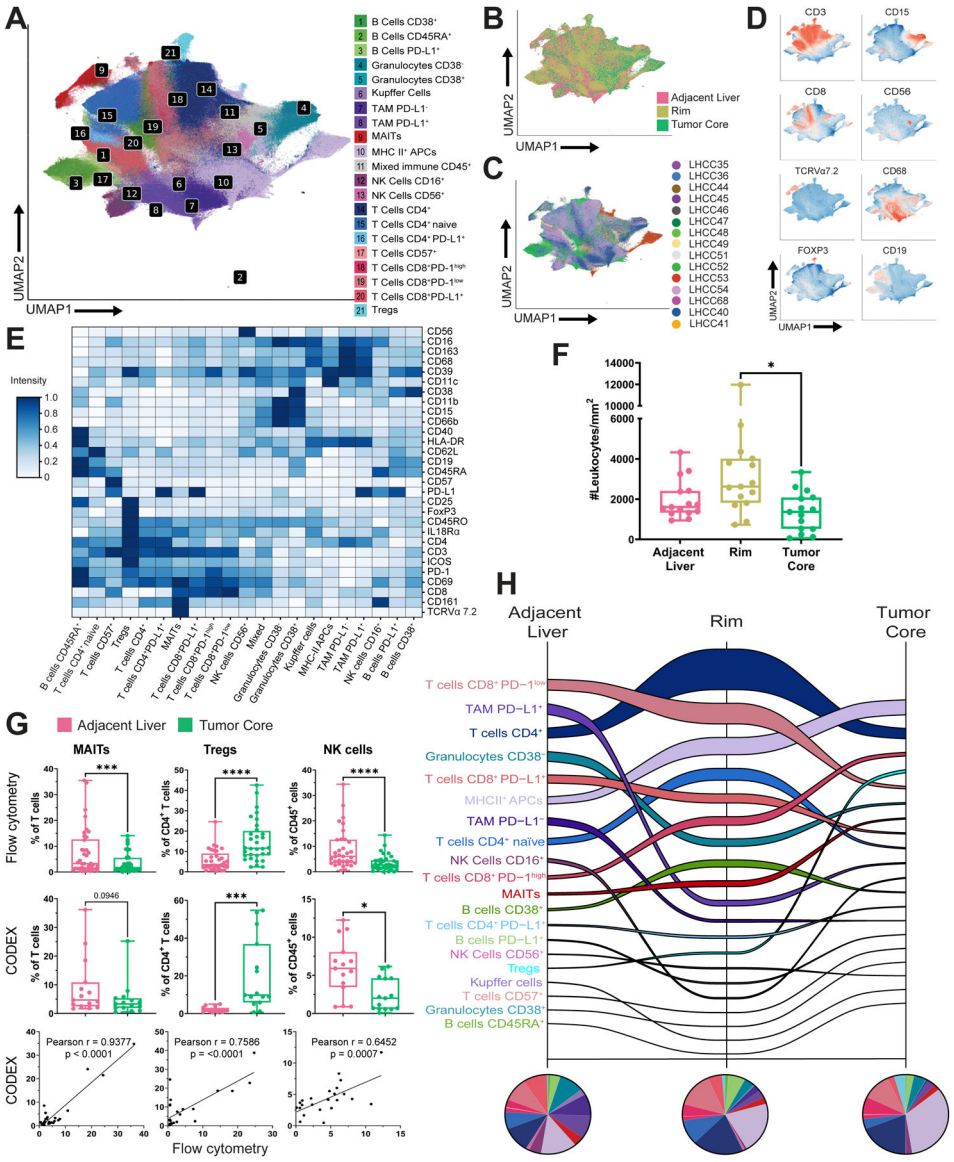

Figure 4: Identification and analysis of spatial distribution of immune cell phenotypes using CODEX imaging.

(A) UMAP plot, color coded for different immune cell types identified by unsupervised clustering of $CD45^+$cells in the CODEX dataset.

(B) & (C) UMAP plots showing origin of single cells color coded by tissue locations **(B,** see also Fig. 3B) and patients (n=15, **C)**.

(D) UMAP projections showing expression of indicated marker proteins per immune cell cluster.

(E) Heatmap showing expression of indicated marker proteins per immune cell cluster (corresponding to **A**).

(F) Comparison of total $CD45^+$ leukocyte density in the three tissue regions.

(G) Correlation of MAIT, T_{reg} and NK cell frequencies as determined by flow cytometry (top panel, n=37) and CODEX (middle panel, n=15). The bottom panel shows correlation of frequencies derived from paired patient samples (n=12) and measured by either flow

cytometry or CODEX. Each datapoint corresponds to a paired measurement in either adjacent liver or tumor core. Pearson r and p values as indicated.

(H) Sankey flow diagram of HCC samples representing indicated immune cell populations sorted on the y-axis from highest (top) to lowest (bottom) cell density in the specified histopathological compartments.The line width is scaled to cell density across the three regions. Pie charts at the bottom represent frequency of different immune cells within each spatial category.

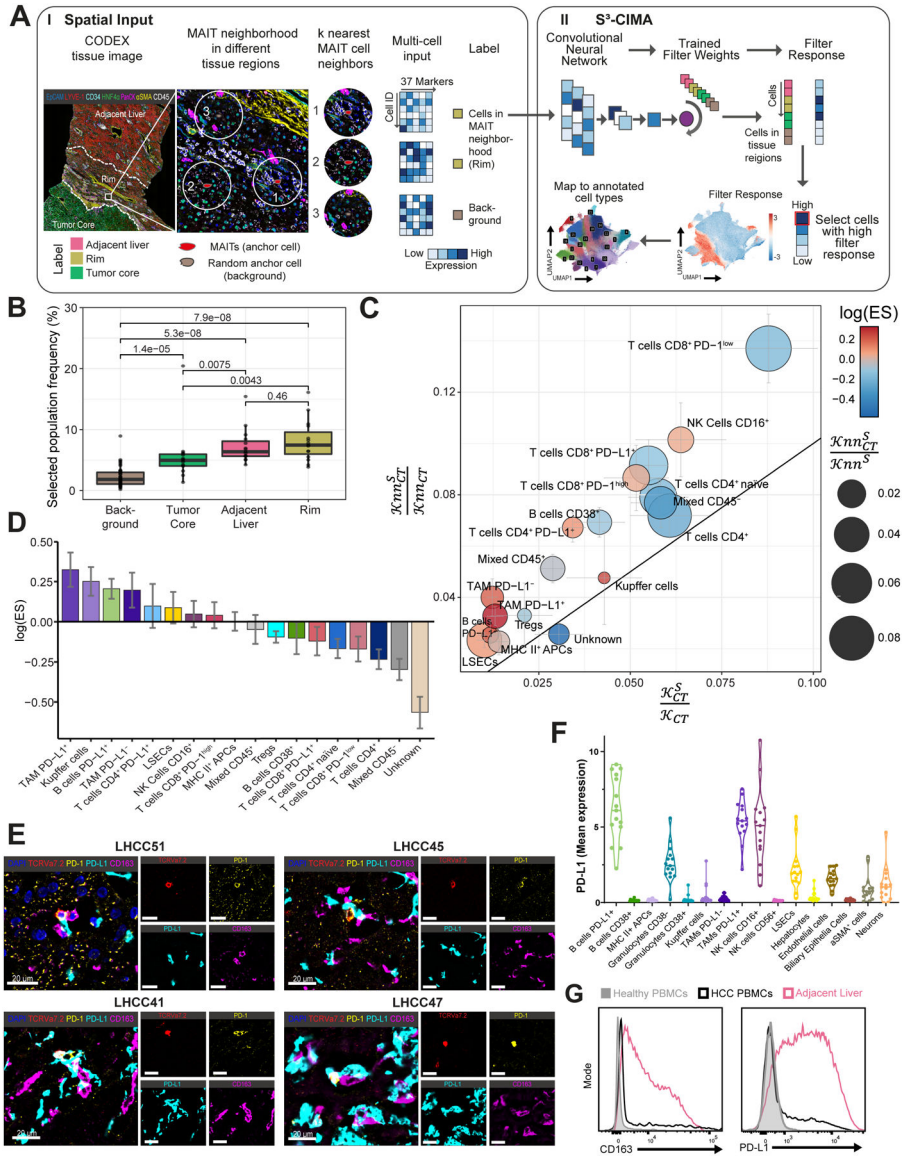

Figure 5: MAIT cell neighborhood analysis identifies the cellular interaction network underlying the immunosuppressive MAIT cell niche

(A) Schematic of S[3]-CIMA (Supervised Spatial Single Cell Imaging Analysis) algorithm used on CODEX single-cell data to investigate the MAIT cell neighborhoods in different tissue regions.

(B) Boxplots showing frequencies of selected cells from different tissue regions compared with randomly selected cells in the background.

(C) Bubble plot displaying S[3]-CIMA classification of cell types in whole tissue sections with neighborhood size k=40 nearest neighboring cells. Y-Axis shows the ratio of the number of all selected cell type CT in nearest neighbor of the anchor cell $(\mathscr{K}nn^{S}_{CT}:)$ to the number of all cell type CT in nearest neighbor of the anchor cell$(\mathscr{K}nn_{CT})$. X-axis shows the ratio of the Number of all selected cell type CT $(\mathscr{K}^{S}_{CT}:)$ to the number of all cells of cell type CT $\mathscr{K}_{CT}$. Color-coding corresponds to the enrichment score (ES) as displayed in **(C).** Size of

the bubble displays the ratio: number of all selected cell type CT in nearest neighbor of the anchor cell $(\mathscr{K}nn^{S}_{CT})$ to the number of all selected cells in nearest neighbor of the anchor cell $\mathscr{K}nn^{S}$ or $\frac{\mathscr{K}nn^{S}_{CT}}{\mathscr{K}nn^{S}}$

(D) Waterfall plot displaying enrichment score of indicated cell populations in the MAIT cell neighborhood (data for adjacent liver is shown) as selected by S^3-CIMA. Values >1 indicate specific enrichment in the MAIT cell niche.

(E) Five-color overlay images of a CODEX datasets displaying interactions between PD-L1$^+$ (turquoise) CD163$^+$ (pink) macrophages and PD-1 (yellow) on MAIT cells (TCRVa7.2$^{+,}$ red) in the adjacent liver. Examples for 4 different patient samples (are shown.

(F) Mean expression of PD-L1 on selected cell populations in the normal liver tissue region as determined by CODEX imaging.

(G) Representative histograms showing M2 polarization of TAMs (defined as CD45$^+$CD68$^+$) as determined by expression of CD163 (left) and PD-L1 (right) on macrophages from healthy PBMCs (grey), HCC patient PBMCs (black), and adjacent, non-tumor tissue (red).

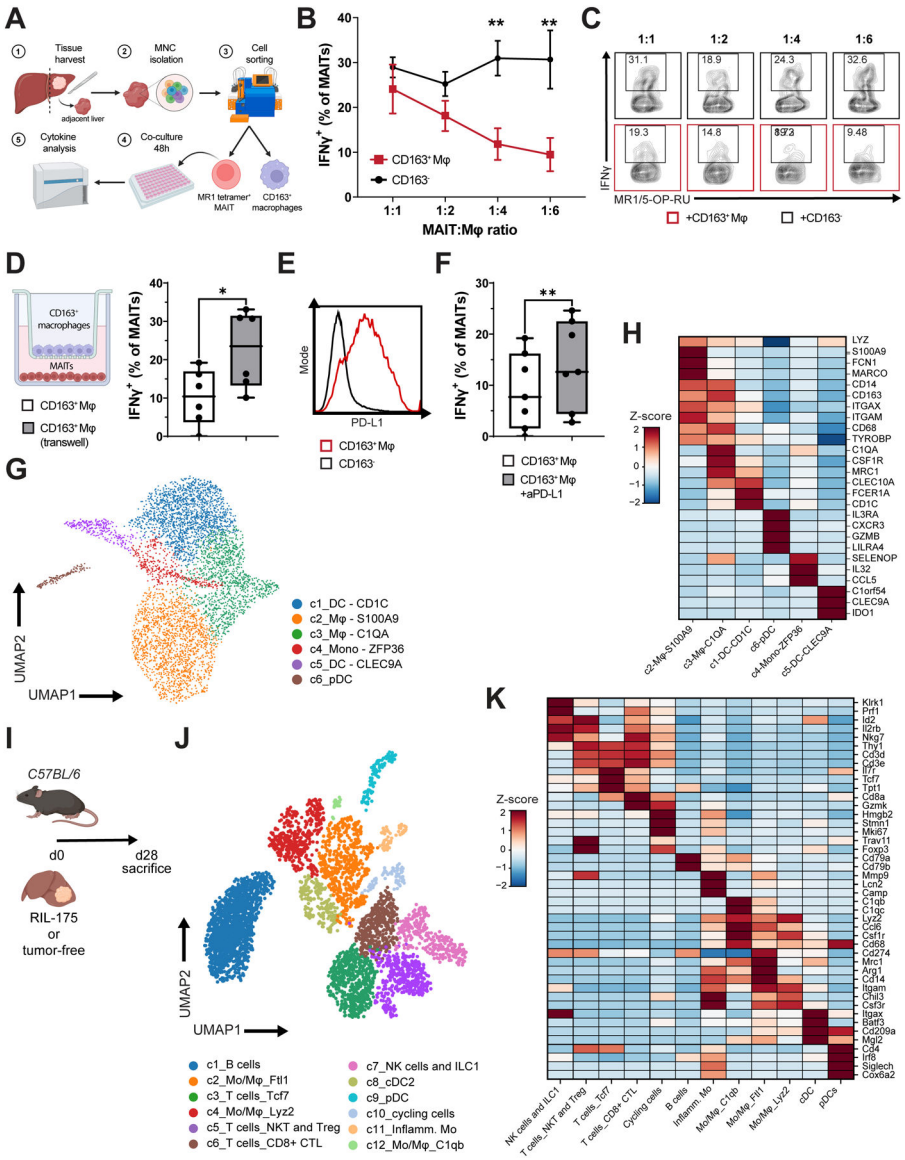

Figure 6: CSF1R^{+}CD163^{+}PD-L1^{+} TAMs impair human MAIT cell function *ex vivo* in a contact and PD-L1 dependent manner.

(A) Experimental setup

(B) Frequency of IFNγ^{+} MAITs after co-culture with CD163^{+} Mφ or CD163^{-} hepatic MNCs at indicated ratios. **(C)** Representative flow cytometry plots. Data include n=7 independent patient samples.

(D) Scheme of the transwell experiment. Box plots shows frequency of IFNγ^{+} MAITs after co-culture with CD163^{+} Mφ at 1:6 ratio either in contact dependent or independent manner. Data include n=6 independent patient samples.

(E) Representative histogram showing PD-L1 expression on sorted CD163^{+}Mφ cells compared to CD163^{-} cells

(F) Box plots shows frequency of IFNγ^{+} MAITs after co-culture with CD163^{+} Mφ at 1:6 ratio in presence or absence of aPD-L1 (20ng/mL). Data include n=7 independent patient samples, n=6 control group samples as in **(D)**.

(G) Hepatic CD45$^+$ sorted myeloid cell clusters from Fig. 1A were selected and reclustered. UMAP projection showing subtypes of myeloid-derived cells and each cluster is color-coded according to the annotations indicated in the figure.

(H) Heatmap projections showing expression of selected indicated marker genes among myeloid cell clusters (corresponding to clusters in **G**)

(I) Experimental setup: C57BL/6 mice were injected orthotopically with syngeneic HCC cell line RIL-175 or left tumor-free. At d28 mice were sacrificed and liver and tumor-infiltrating MNCs were isolated. CD45$^+$ sorted cells were subsequently subjected to single-cell RNA-sequencing.

(J) UMAP projection showing the landscape of murine CD45$^+$ cells pooled from tumor-free and tumor-bearing animals.

(K) Heatmap projections showing expression of selected indicated marker genes among murine immune cell clusters (corresponding to clusters in **J**)

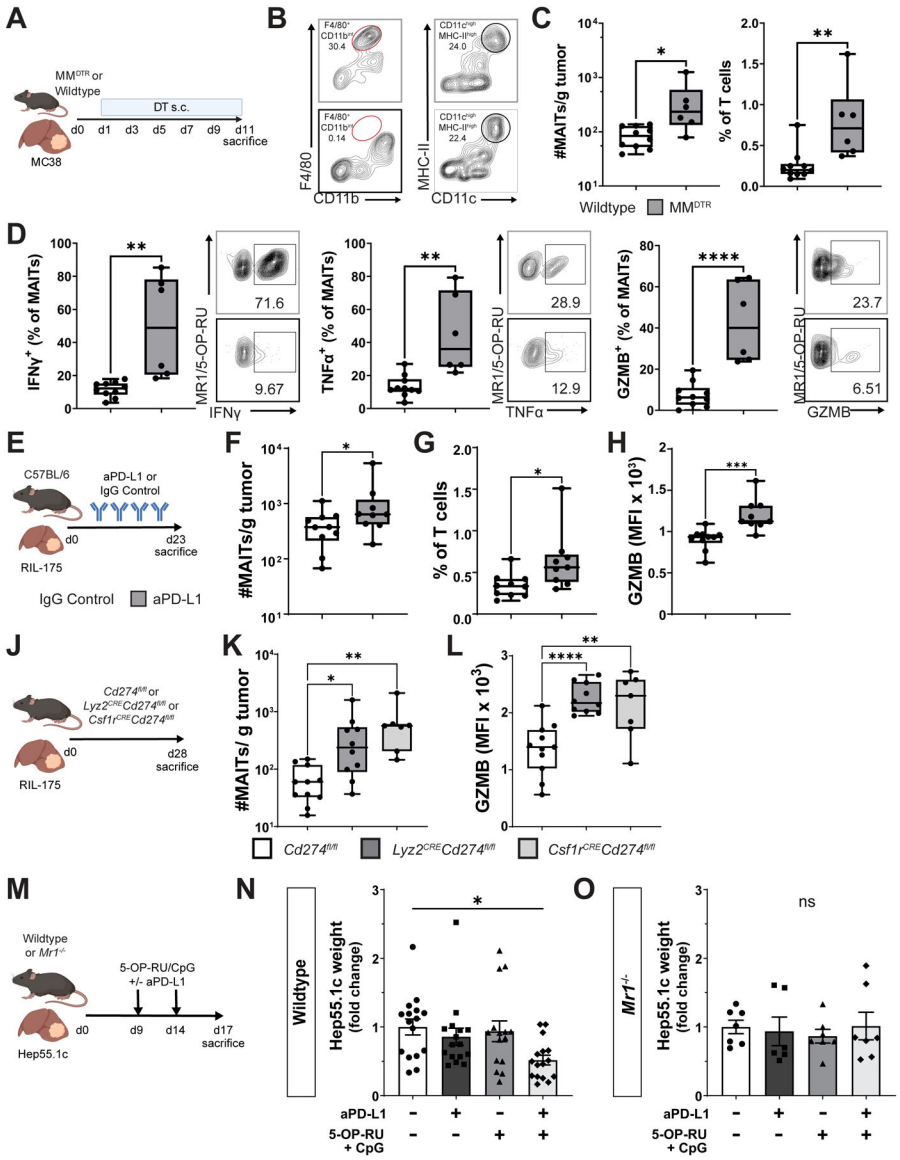

Figure 7: MAIT dysfunction in murine HCC is reversed by PD-L1 blockade *in vivo* and by depletion of CSF1R^{+} TAMs.

(A) MC38 tumor-bearing, transgenic MM^{DTR} or wildtype mice received DT (250ng/mouse) s.c. every other day starting d1.

(B) Representative flow plot showing frequency of hepatic F4/80^{+}/CD11b^{int} macrophages (gated on CD45^{+}CD3^{-}CD19^{-}NK1.1^{-}) or CD11c^{+}MHC-II^{+} cDC (gated on CD45^{+}CD3^{-}CD19^{-}NK1.1^{-}F4/80^{-}) for MM^{DTR} or WT mice after injection of DT.

(C) On d11, tumors were harvested, and the cell number (left) and frequency (right) of tumor infiltrating MAIT cells was determined. Comparison between Wildtype (n=10) vs MM^{DTR} mice (n=6).

(D) Experimental setup as in **(A)**. Boxplots summarizing cytokine expression of intrahepatic MAIT cells for IFN γ, granzyme B, and TNFα after 4h of *ex vivo* stimulation.. Representative flow cytometry dot plots are shown. Comparison between Wildtype (n=10) vs MM^{DTR} mice (n=6) is shown.

(E) RIL-175 tumor-bearing C57BL/6 mice received aPD-L1 or IgG control i.p. at d5, d10, d15 & d20.

(F&G) On d23, tumors were harvested, and the cell number **(F)** and frequency **(G)** of tumor infiltrating MAIT cells was determined by flow cytometry. Comparison between IgG Control (n=10) vs aPD-L1 (n=9) is shown.

(H) Experimental setup as in **(E)** granzyme B expression of intrahepatic MAIT cells after 4h of *ex vivo* stimulation. Comparison between IgG Control and aPD-L1 i.p. treatment.

(J) $Cd274^{fl/fl}$ (Control), $Lyz2^{CRE}Cd274^{fl/fl}$ and $Csf1r^{CRE}Cd274^{fl/fl}$ lines received RIL=175 intrahepatic and livers and tumors were harvested on d28.

(K) Tumors were harvested, and the number of tumor- infiltrating MAIT cells was determined by flow cytometry. n=11 for $Cd274^{fl/fl}$, n=10 for $Lyz2^{CRE}Cd274^{fl/fl}$ and n=7 *Csf1rCRECd274fl/fl*

(L) Boxplots showing MFI of granzyme B **(K)** in hepatic MAIT cells after 4h of *ex vivo* stimulation. Comparisons as in **(L)**.

(M) C57BL/6 or $Mr1^{-/-}$ mice received intrahepatic injection of syngeneic HCC cell line Hep55.1c. 5-OP-RU/CpG treatment and/or aPD-L1 was administered intraperitoneally at indicated time points.

(N&O) Bar graphs showing fold change of Hep55.1c tumor weights at d17 in comparison to the mean tumor weight of the control treated C57BL/6 (Wildtype) **(N)** or $Mr1^{-/-}$ mice **(O)**.

KEY RESOURCES TABLE

REAGENT or RESOURCE	SOURCE	IDENTIFIER
Antibodies		
Alexa Fluor® 700 Anti-Human CD45 (Clone HI30)	BioLegend	Cat #: 304023; RRID: AB_493760
V500 Mouse Anti-Human CD14 (Clone M5E2)	BD Biosciences	Cat #: 561391; RRID: AB_10611856
V500 Mouse Anti-Human CD15 (Clone HI98)	BD Biosciences	Cat #: 561585; RRID: AB_10896278
V500 Mouse Anti-Human CD19 (Clone HIB19)	BD Biosciences	Cat #: 561125; RRID: AB_10563208
PerCP/Cyanine5.5 Anti-Human CD3 (Clone UCHT1)	BioLegend	Cat #: 300430; RRID: AB_893299
BB515 Mouse Anti-Human CD14 (Clone RPA-T4)	BD Biosciences	Cat #: 564419; RRID: AB_2744419
Brilliant Violet 605™ Anti-Human CD8a (Clone RPA-T8)	BioLegend	Cat #: 301040; RRID: AB_2563185
PE Anti-Human TCR Va7.2 (Clone 3C10)	BioLegend	Cat #: 351706; RRID: AB_10899577
PE/Cyanine7 Anti-Human CD161 (Clone HP-3G10)	BioLegend	Cat #: 339918; RRID: AB_11126745
APC/Fire™ 750 Anti-Human CD56 (NCAM) Recombinant (Clone QA17A16)	BioLegend	Cat #: 392408; RRID: AB_2728404
PE-CD594 Mouse Anti-Human CD69 (Clone FN50)	BD Biosciences	Cat #: 562645; RRID: AB_2737699
APC Anti-Human CD25 (Clone BC96)	BioLegend	Cat #: 302610; RRID: AB_314280
Brilliant Violet 650™ Anti-Human CD38 (Clone HB-7)	BioLegend	Cat #: 356620; RRID: AB_2566233
Brilliant Violent 421™ Anti-Human CD279 (PD-1) (Clone: EH12.2H7)	BioLegend	Cat #: 329920; RRID: AB_10960742
BV650 Mouse Anti-Human CD274 (Clone: MIH1)	BD Biosciences	Cat #: 563740; RRID: AB_2738398
Brilliant Violent 785™ Anti-Human HLA-DR (Clone: CL243)	BioLegend	Cat #: 307641; RRID: AB_2561360
PE anti-human CD206 (MMR) Antibody	BioLegend	Cat #: 321106; RRID: AB_571911
APC Mouse Anti-Human CD14 (CLONE M5E2)	BD Biosciences	Cat #: 561383; RRID: AB_10612009
PerCP/Cy5.5 Anti-Human CD11b (Clone: ICRF44)	BioLegend	Cat #: 301327; RRID: AB_10900072
FITC Mouse Anti-Human CD163 (Clone GHI/61)	BD Biosciences	Cat #: 563697; RRID: AB_2738379
BV421 Mouse Anti-Human CD3 (Clone UCHT1)	BD Biosciences	Cat #: 562426; RRID: AB_11152082
Brilliant Violet 421™ Anti-Human CD19 (Clone HIB19)	BioLegend	Cat #: 302234; RRID: AB_11142678
PE/Cy™7 Mouse Anti-Human CD68 (Clone Y1/82A)	BD Biosciences	Cat #: 565595; RRID: AB_2739298

REAGENT or RESOURCE	SOURCE	IDENTIFIER
BV510 Mouse Anti-Human CD11c (Clone: B-ly6)	BD Biosciences	Cat #: 563026; RRID: AB_2737960
BD Pharmingen™ APC Mouse Anti-Human IFN-γ	BD Biosciences	Cat#: 554702 RRID: AB_398580
Human BD Fc Block™	BD Biosciences	Cat #: 564220; RRID: AB_2728082
Purified anti-mouse CD16/32 Antibody	BioLegend	Cat #: 101302; RRID: AB_312800
PerCP/Cyanine5.5 anti-mouse CD62L Antibody (Clone: MEL-14)	BioLegend	Cat #: 104432, RRID: AB_2285839
PE/Cyanine7 anti-mouse/human CD44 Antibody (Clone: IM-7)	BioLegend	Cat #: 103030, RRID: AB_830787.
Brilliant Violet 650™ anti-mouse CD69 Antibody (Clone: H1.2F3)	BioLegend	Cat #: 104541, RRID: AB_2616934
APC/Fire™ 750 anti-mouse TCR β chain Antibody (Clone: H57–597)	(BioLegend	Cat #: 109246, RRID: AB_2629697
PE anti-mouse NK-1.1 Antibody (Clone: PK136)	BioLegend	Cat #: 108708, RRID: AB_313395
Alexa Fluor® 700 anti-mouse F4/80 Antibody (Clone: BM8)	BioLegend	Cat #: 123130, RRID: AB_2293450
Alexa Fluor® 700 anti-mouse/human CD45R/B220 Antibody (Clone: RA3–6B2)	BioLegend	Cat #: 103232, RRID: AB_493717
Alexa Fluor® 700 anti-mouse/human CD11b Antibody (Clone: M1-70)	BioLegend	Cat #: 101222, RRID: AB_493705
Alexa Fluor® 594 anti-mouse CD3 Antibody (Clone: 17A2)	BioLegend	Cat #: 100240, RRID: AB_2563427
Brilliant Violet 605™ anti-mouse CD4 Antibody (Clone: GK1.5)	BioLegend	Cat #: 100451, RRID: AB_2564591
Alexa Fluor® 700 Rat Anti-Mouse CD4 (Clone: RM4–5)	BD Biosciences	Cat #: 557956, RRID: AB_396956
BV786 Rat Anti-Mouse CD8a (Clone: 53–6.7)	BD Biosciences	Cat #: 563332, RRID: AB_2721167
Pacific Blue™ anti-mouse/human CD11b Antibody (Clone: M1/70)	BioLegend	Cat #: 101224, RRID: AB_755986
Alexa Fluor® 700 anti-mouse Ly-6G Antibody (Clone: 1A8)	BioLegend	Cat #: 127622, RRID: AB_10643269
APC/Cyanine7 anti-mouse Ly-6C Antibody (Clone: HK1.4)	BioLegend	Cat #: 128026, RRID: AB_10640120
Brilliant Violet 421™ anti-mouse Ki-67 Antibody	BioLegend	Cat# 652411, RRID: AB_2562663
ROR gamma (t) Monoclonal Antibody (B2D), PE, eBioscience™	Thermo Fisher Scientific	Cat# 12–6981–82, RRID: AB_10807092
PE/Cyanine7 anti-T-bet Antibody	BioLegend	Cat# 644824, RRID: AB_256176
FOXP3 Monoclonal Antibody, APC, eBioscience™ (Clone: FJK-16s)	Thermo Fisher Scientific	Cat #: 17–5773–82, RRID: AB_469457)
APC anti-mouse IFN-γ Antibody (Clone: XMG1.2)	BioLegend	Cat #: 505810, RRID: AB_315404
APC anti-mouse Perforin Antibody (Clone: S16009A)	BioLegend	Cat #: 154304, RRID: AB_2721463

REAGENT or RESOURCE	SOURCE	IDENTIFIER
FITC anti-human/mouse Granzyme B Antibody (Clone: GB11)	BioLegend	Cat #: 515403, RRID: AB_2114575
FITC anti-mouse IL-17A Antibody (Clone: TC11–18H10.1)	BioLegend	Cat #: 506908, RRID: AB_536010
CD45-BX001 (HI30)—ALEXA FLUOR™ 488-RX001 Kit (Clone: HI30)	Akoya Biosciences	Cat #: 4150003; RRID: AB_2895052
CD8-BX004 (SK1)—ALEXA FLUOR™ 488-RX004 Kit (Clone: SK1)	Akoya Biosciences	Cat #: 4150004; RRID: AB_2895049
CD38 comm (Clone: HB-7)	Akoya Biosciences	Cat #: 4150007; RRID: AB_2909414
Purified anti-human CD45RO (Maxpar(R) Ready) antibody (Clone: UCHL1)	Biolegend	Cat #: 304239; RRID: AB_2563752
pancytokeratin comm (Clone: AE-1/AE-3)	Akoya Biosciences	Cat #: 4150020; RRID: AB_2909509 (TEMPORARY)
Purified anti-human CD39 (Maxpar(R) Ready) antibody (Clone: A1)	Biolegend	Cat #: 328221; RRID: AB_2563747
Purified anti-human CD15 (SSEA-1) antibody (Clone: HI98)	Biolegend	Cat #: 301902; RRID: AB_314194
Purified anti-human CD40 antibody (Clone: HB14)	Biolegend	Cat #: 313002; RRID: AB_314965
Purified anti-CD68 antibody (Clone: KP1)	Biolegend	Cat #: 916104; RRID: AB_2616797
FOXP3 Monoclonal Antibody (PCH101), eBioscience (Clone: PCH101)	ThermoFisher	Cat #: 14–4776–82; RRID: AB_467554
Purified anti-human CD163 antibody (Clone: GHI/61)	Biolegend	Cat #: 333602; RRID: AB_1088991
Anti-CD56 Monoclonal Antibody, Unconjugated (Clone: 123.C3.5D)	Cell Marque	Cat #: 156M-86; RRID: AB_1158184
Purified anti-human CD326 (Ep-CAM) antibody (Clone: 9C4)	Biolegend	Cat #: 324202; RRID: AB_756076
Purified anti-human CD66b antibody (Clone: G10F5)	Biolegend	Cat #: 305102; RRID: AB_314494
Purified anti-human CD25 antibody (Clone: M-A251)	Biolegend	Cat #: 356102; RRID: AB_2561752
Anti-Human CD62L - Purified (CODEX® Ready) antibody (Clone: DREG56)	Leinco	Cat #: C512–50 μg; RRID: AB_2893569
CD279 comm (Clone: EH12.2H7)	Akoya Biosciences	Cat #: 4250010; RRID: AB_2909510
ICOS comm (Clone: C398.4A)	Akoya Biosciences	Cat #: 4250013; RRID: AB_2909511
LEAF™ Purified anti-human CD11b antibody (Clone: ICRF44)	Biolegend	Cat #: 301312; RRID: AB_314164
HNF-4alpha (H-1) antibody (Clone: H-1)	Santa Cruz	Cat #: sc-374229; RRID: AB_10989766
HLA-DR-BX026 (L243)—ATTO 550-RX026 Kit (Clone: L243)	Akoya Biosciences	Cat #: 4250006; RRID: AB_2895054
Purified anti-human CD161 antibody (Clone: HP-3G10)	Biolegend	Cat #: 339902; RRID: AB_1501090
Goat Anti-Human Il-18 r alpha / il-1 r5 Polyclonal antibody, Unconjugated (Clone: goat polyclonal)	R&D Systems	Cat #: AF840; RRID: AB_355650

REAGENT or RESOURCE	SOURCE	IDENTIFIER
CD34 comm (Clone: 561)	Akoya Biosciences	Cat #: 4250020; RRID: AB_2909512 (TEMPORARY)
CD69 comm (Clone: FN50)	Akoya Biosciences	Cat #: 4250022; RRID: AB_2909513 (TEMPORARY)
KI67-BX047 (B56)—ATTO 550-RX047 Kit (Clone: B56)	Akoya Biosciences	Cat #: 4250019; RRID: AB_2895046
CD19-BX003 —CY5-RX003 (Clone: HIB19)	Akoya Biosciences	Cat #: 4350003
Anti-Human CD19 - Purified In vivo GOLD™ Functional Grade antibody (Clone: SJ25-C1)	Leinco	Cat #: C2854–1.0 mg; RRID: AB_2829610
PD-L1 (E1L3N) XP Rabbit Antibody (Clone: E1L3N)	Cell Signalling	Cat #: 13684S; RRID: AB_2687655
CD3-BX015 (UCHT1)—CY5-RX015 Kit (Clone: UCHT1)	Akoya Biosciences	Cat #: 4350008; RRID: AB_2895047
CD4-BX021—CY5-RX021 Kit (Clone: SK3)	Akoya Biosciences	Cat #: 4350010 RRID: AB_2895048
LEAF™ Purified anti-human CD4 antibody (Clone: OKT4)	Biolegend	Cat #: 317404; RRID: AB_571961
Purified anti-human CD57 antibody (Clone: HNK-1)	Biolegend	Cat #: 359602; RRID: AB_2562403
CD11C-BX027 —CY5-RX027 Kit (Clone: S-HCL-3)	Akoya Biosciences	Cat #: 4350012; RRID: AB_2895050
Anti-Human CD16 - FITC antibody (Clone: 3G8)	Leinco	Cat #: C6854; RRID: AB_2893584
Purified anti-human TCR Valpha7.2 antibody (Clone: 3C10)	Biolegend	Cat #: 351702; RRID: AB_10900258
Alpha-Smooth Muscle Actin Monoclonal Antibody, eBioscience (Clone: 1A4)	ThermoFisher	Cat #: 14–9760–82; RRID: AB_2572996
LYVE1 antibody (Clone: polyclonal)	Abcam	Cat #: ab36993; RRID: AB_2138663
Mouse Anti-CD45RA Monoclonal Antibody, Unconjugated (Clone: HI100)	BD Biosciences	Cat #: 555486; RRID: AB_395877
Biological samples		
Patient HCC core samples	This paper	N/A
Patient HCC rim samples	This paper	N/A
Patient HCC adjacent normal liver tissue	This paper	N/A
Control liver tissue from patients undergoing liver transplantation	This paper	N/A
Chemicals, peptides, and recombinant proteins		
2-methylbutane	FisherScientific	Cat #: AC167840010; CAS #: 78–78–4
Optimal cutting temperature (O.C.T.) compound	FisherScientific	Cat #: 23–730–571
MACS tissue storage solution	Miltenyi Biotec	Cat #: 130–100008
Serum-free RPMI 1640	Thermofisher	Cat #: 61870127
Collagenase IV	STEMCELL technologies	N/A

REAGENT or RESOURCE	SOURCE	IDENTIFIER
DNAse I	STEMCELL Technologies	Cat #: 07900
Percoll PLUS solution (in PBS)	GE Healthcare	Cat #: GE17–544501
RBC lysis buffer	ThermoFisher	Cat #: 50–1129751
Recovery™ Cell Culture Freezing Medium	Gibco	Cat #: 12648010
FACS buffer	BD Biosciences	Cat #: 554656
Stain Buffer (FBS)	BD Biosciences	Cat #: 564220; RRID: AB_2869006
Fixable Viability dye ZOMBIE-UV	BioLegend	Cat #: 423108
Acridine Orange / Propidium Iodide Stain	Logos Biosystems	F23001
RPMI 1640 Medium, GlutaMAX™ Supplement	ThermoFisher	Cat #: 61870127
Corning™ Regular Fetal Bovine Serum	Corning	Cat #: MT35010CV
Sodium Pyruvate 100 mM	ThermoFisher	Cat #: 11360070
HEPES (1M)	ThermoFisher	Cat #: 15630080
MEM Non-Essential Amino Acids Solution (100X)	ThermoFisher	Cat #: 11140050
Puromycin	InvivoGen	Cat #: ant-pr-1; CAS #: 58–58–2
Corning® Matrigel® Growth Factor Reduced (GFR) Basement Membrane Matrix, LDEV-free, 10 mL	Coning	Cat #: 354230
Percoll	Cytiva	Cat #: 17089109
Lympholyte Cell Separation Media	Cedarlane Laboratories	Cat. No. CL5035
ACK-lysis buffer	Quality Biologicals	Cat #: 118–156–101
Murine and human MR1-tetramers loaded with MAIT ligand 5-OP-RU	NIH Tetramer Core	NA
Leukocyte Activation Cocktail, with BD GolgiPlug™	BD Biosciences	Cat #: 550583, RRID: AB_2868893
eBioscience™ Intracellular Fixation & Permeabilization Buffer Set	ThermoFisher	Cat #: 88–8824–00
Critical commercial assays		
N/A		
Deposited data		
CRISPR/Cas9 lentiviral vector targeting murine Cd274	This paper	Addgene ID: 199279
GRCh38 reference		refdata-gex-mm10-2020-A
GRCh38 VDJ reference		refdata-cellranger-vdj-GRCh38-alts-ensembl-5.0.0
Transcriptomic data of 371 patients diagnosed with HCC	The Cancer Genome Atlas Project- LIHC cohort	https://cancergenome.nih.gov/
scRNA-seq Data from human HCC patients	This paper	The database of Genotypes and Phenotypes (dbGaP); Accession number: phs003279.v1.p1
scRNA-seq Data from murine tumor-bearing vs tumor-free livers	This paper	GEO: GSE231712
CODEX images	This paper	The Canccer imaging Archives (TCIA)

REAGENT or RESOURCE	SOURCE	IDENTIFIER
		under https://doi.org/10.7937/bh0r-y074
Sc-RNA-seq data HCC patients + ICB	Ma et al., 2021	GEO: GSE12544
Experimental models: Cell lines		
Luciferase-expressing RIL-175	Kapanadze et al., 2013	N/A
Syngeneic Hep55.1c	CLS Cell Lines Service GmbH	Cat #: 400201
B16F10 (GFP and luciferase-expressing)	Kreiter et al., 2015	N/A
MC38	Dr, Jay Berzofsky (NCI)	RRID:CVCL_B288
Experimental models: Organisms/strains		
NCI C57BL/6NCr Mice	Charles River Laboratories	Code: 556
Mr1$^{-/-}$ mice	Treiner et al., 2013	N/A
Lyz2^{Cre} mice	Jackson Laboratory	Strain#: strain #004781
Csf1r$^{LsL\text{-}DTR}$mice	Jackson Laboratory	Strain#: 024046
Csf1r^{Cre} mice	Jackson Laboratory	Strain#: 029206
Cd274$^{fl/fl}$	Jackson Laboratory	Strain #: 036255
Oligonucleotides		
Primer: MR1 5 8763–8783: AGC TGA AGT CTT TCC AGA TCG,	Ruf et al., 2021	N/A
Primer: MR1 9188–9168 rev: ACA GTC ACA CCT GAG TGG TTG	Ruf et al., 2021	N/A
Primer: MR1 10451–1043: GAT TCT GTG AAC CCT TGC TTC	Ruf et al., 2021	N/A
BX001—Alexa Fluor™ 488-RX001	Akoya Biosciences	Cat #: 5450013
BX004—Alexa Fluor™ 488-RX004	Akoya Biosciences	Cat #: 5450014
BX007—Alexa Fluor™ 488-RX007	Akoya Biosciences	Cat #: 5450015
BX010—Alexa Fluor™ 488-RX010	Akoya Biosciences	Cat #: 5450016
BX013—Alexa Fluor™ 488-RX013	Akoya Biosciences	Cat #: 5450017
BX016—Alexa Fluor™ 488-RX016	Akoya Biosciences	Cat #: 5150001
BX019—Alexa Fluor™ 488-RX019	Akoya Biosciences	Cat #: 5150002
BX022—Alexa Fluor™ 488-RX022	Akoya Biosciences	Cat #: 5150003
BX025—Alexa Fluor™ 488-RX025	Akoya Biosciences	Cat #: 5150004
BX028—Alexa Fluor™ 488-RX028	Akoya Biosciences	Cat #: 5150005
BX031—Alexa Fluor™ 488-RX031	Akoya Biosciences	Cat #: 5150006
BX034—Alexa Fluor™ 488-RX034	Akoya Biosciences	Cat #: 5150007
BX037—Alexa Fluor™ 488-RX037	Akoya Biosciences	Cat #: 5150008
BX040—Alexa Fluor™ 488-RX040	Akoya Biosciences	Cat #: 5150009
BX043—Alexa Fluor™ 488-RX043	Akoya Biosciences	Cat #: 5150010
BX046—Alexa Fluor™ 488-RX046	Akoya Biosciences	Cat #: 5150011
BX049—Alexa Fluor™ 488-RX049	Akoya Biosciences	Cat #: 5150012

REAGENT or RESOURCE	SOURCE	IDENTIFIER
BX002—Atto 550-RX002	Akoya Biosciences	Cat #: 5450023
BX005—Atto 550-RX005	Akoya Biosciences	Cat #: 5450024
BX014—Atto 550-RX014	Akoya Biosciences	Cat #: 5450025
BX017—Atto 550-RX017	Akoya Biosciences	Cat #: 5250001
BX020—Atto 550-RX020	Akoya Biosciences	Cat #: 5250002
BX023—Atto 550-RX023	Akoya Biosciences	Cat #: 5250003
BX026—Atto 550-RX026	Akoya Biosciences	Cat #: 5250004
BX029—Atto 550-RX029	Akoya Biosciences	Cat #: 5250005
BX032—Atto 550-RX032	Akoya Biosciences	Cat #: 5250006
BX035—Atto 550-RX035	Akoya Biosciences	Cat #: 5250007
BX041—Atto 550-RX041	Akoya Biosciences	Cat #: 5250008
BX047—Atto 550-RX047	Akoya Biosciences	Cat #: 5250009
BX003—Cy5-RX003	Akoya Biosciences	Cat #: 5450026
BX006—Cy5-RX006	Akoya Biosciences	Cat #: 5450027
BX015—Cy5-RX015	Akoya Biosciences	Cat #: 5350001
BX021—Cy5-RX021	Akoya Biosciences	Cat #: 5350002
BX024—Cy5-RX024	Akoya Biosciences	Cat #: 5350003
BX027—Cy5-RX027	Akoya Biosciences	Cat #: 5350004
BX030—Cy5-RX030	Akoya Biosciences	Cat #: 5350005
BX033—Cy5-RX033	Akoya Biosciences	Cat #: 5350006
BX036—Cy5-RX036	Akoya Biosciences	Cat #: 5350007
BX042—Cy5-RX042	Akoya Biosciences	Cat #: 5350008
BX045—Cy5-RX045	Akoya Biosciences	Cat #: 5350009
Software and algorithms		
10x Genomics Cell Ranger pipeline (v5.0 or v6.0)	10x Genomics	N/A
S3-CIMA	Babaei et al.2023	https://github.com/claassenlab/S3-CIMA
Visreg R package	Breheny and Burchett, 2013	N/A
HALO image analysis platform V3.2	Indica Labs	N/A
ImageJ (Fiji version 2.8.5)	NIH	N/A
FlowJo	FlowJo	RRID: SCR_008520
GraphPad Prism 9	GraphPad Prism	RRID: SCR_002798
Other		
LUNA-FL fluorescent cell counter	Logos Biosystems	N/A
10x Genomics Chromium platform, 5’ v1.1 immune profiling chemistry	10x Genomics	PN-1000165
Illumina NextSeq 550 instrument	Illumina	N/A
Illumina NextSeq 2000 instrument	Illumina	N/A
gentleMACS Octo Dissociator Tissue Dissociator	Miltenyi	RRID: SCR_020272

REAGENT or RESOURCE	SOURCE	IDENTIFIER
CytoFLEX LX flow cytometer	Beckman Coulter	RRID: SCR_019627